Contributions of sub-community based on short and long-range white matter tracts in personalized age-associated neurocompensatory mechanism

Priyanka Chakraborty[1,2], Suman Saha[1], Arpan Banerjee[1], Dipanjan Roy[†1,3]

[1]Cognitive Brain Dynamics Lab, National Brain Research Centre, NH-8, Manesar, Haryana 122051, India

[2]Department of Mathematics, Rampurhat College, Rampurhat, West Bengal 731224, India

[3]School of AIDE, Center for Brain Science and Applications, IIT Jodhpur, NH-62, Surpura Bypass Rd, Karwar, Rajasthan 342030, India

Corresponding authors : [†]droy@iitj.ac.in

Abstract

Brain function is shaped by the local and global connections between its dynamical units and biological parameters. As we age, the anatomical topology undergoes significant deterioration (e.g., long-range white matter fiber loss) that affects the brain's overall function. Despite the structural loss, existing studies have pinpointed that normative patterns of functional integrity, defined as the compensatory mechanism of the aging brain, remain intact across the lifespan. However, the crucial components in guiding the adaptive mechanism by which the brain readjusts its biological parameters to maintain optimal compensatory function with age still needs to be uncovered. Here, we provide a parsimonious mechanism, which, together with the data-driven whole-brain generative model, establishes an individualized structure-function link with aging, and uncover sub-communities' role in driving the neurocompensation process. We use two neuroimaging datasets of healthy human cohorts with large sample sizes to systematically investigate which of the brain sub-graphs (connected via short- or long-range white-matter tracts) drives the compensatory mechanisms and modulates intrinsic global scaling parameters, such as interaction strength and conduction delay, in preserving functional integrity. The functional integrity is evaluated under the hypothesis of preserved metastability, measured from individuals' fMRI BOLD signals. Our findings uncover that the sub-graph connected via short-range tracts mainly modulates global coupling strength to compensate for structural loss. In contrast, long-range connections contribute to the conduction delay, which may play a complementary role in neurocompensation. For the first time, these findings shed light on the underlying neural mechanisms of age-related compensatory mechanisms and provide a mechanistic explanation for the importance of short-range connections in the face of the loss of long-range connections during aging using BOLD fMRI data. This crucial insight could open avenue to understand the role of subgraphs for targeted interventions to address aging-associated neurodegenerative diseases where long-range connections are significantly deteriorated.

Keywords: Aging, tract length, short- and long-range connections, metastability, neurocompensation

1 Introduction

An overarching question in neuroscience concerns how the brain modulates its biological parameters in response to the age-related deterioration of white matter tracts in preserving functional integrity. Particularly, it is unclear how the two

sub-graphs, interacting via short-range (local) or long-range (distant) in the brain, contribute to the neurocompensation to maintain its desired set point [Deco and Kringelbach, 2016, Deco et al., 2017, Naik et al., 2017, Naskar et al., 2021].

Aging is a complex biological process that is associated with degradation of white matter tracts (a reduction in myelin density, axonal degeneration, and decline in tract numbers) [Peters, 2006, Betzel et al., 2014, Lim et al., 2015, Coelho et al., 2021], gray matter volume [Sullivan and Pfefferbaum, 2006], alteration in neurotransmitter levels [Roalf et al., 2020], and changes in large scale brain networks' coordination leading to cognitive and behavioral impairments [Li et al., 2020]. It is well known that the impact of aging on brain function is nonlinear and diverse, vary person to person, leading to the deterioration of some functions [Grady et al., 2010], while few other functions, such as inductive reasoning, verbal fluency, and executive attention, may even improve with age [Salthouse, 2012, Veríssimo et al., 2022]. A representative bridge among the aging , its effects, neurocompensation and the useful measures is shown in Fig. 1. The aging trajectory is placed in Fig. 1(a). The prominent effect of aging are separated into anatomy (Figs. 1(b,c)) and brain functions (Figs. 1(d,e)).

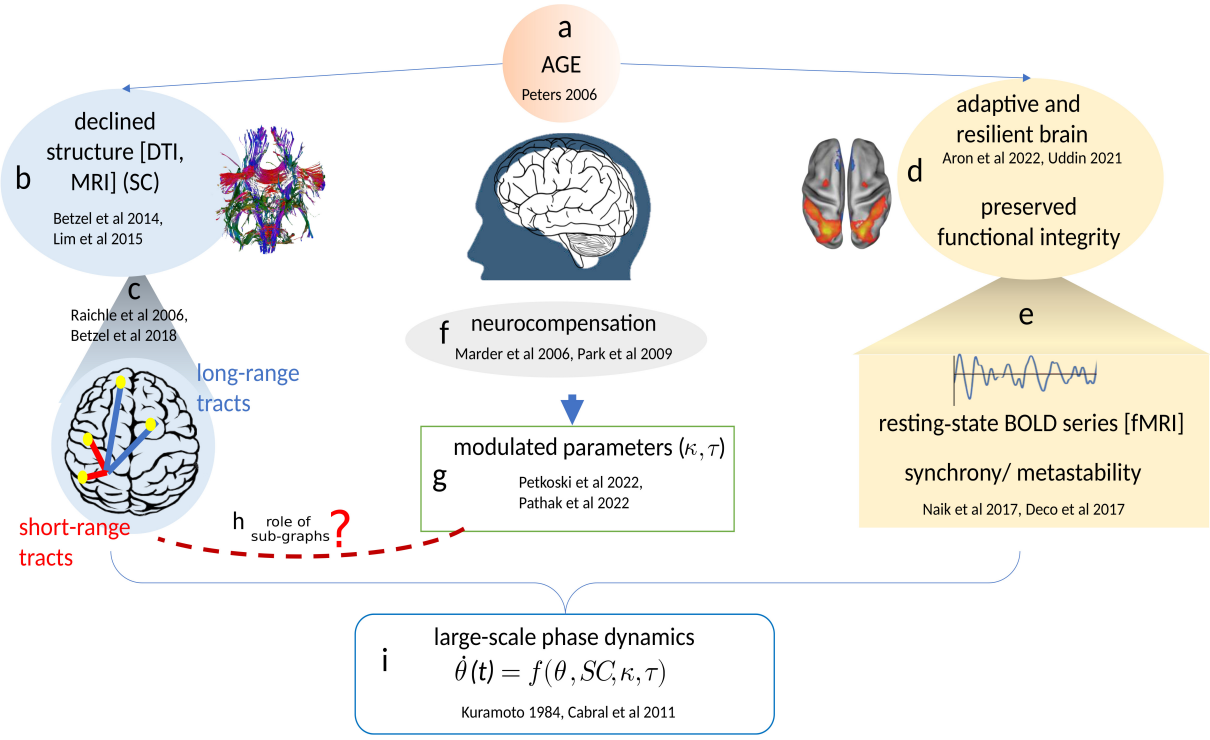

Figure 1: Visual abstract. (a) As we age, the structure of our brains undergoes significant changes that affect their overall function. (b) Research has shown a decline in the structural topology of the brain, (c) including alterations in both short-range and long-range connections. (d) Studies have shown that the brain's functional integrity remains preserved across age despite these structural changes. (e) Resting state BOLD signals, a non-invasive technique, is used to observe large-scale global dynamics. This allows researchers to measure functional quantities such as the global coherence and metastability of the brain's system. Metastability measures the brain's ability to adapt and reorganize its connections over time. The measures are relatively stable across the lifespan, indicating that the brain maintains its functional integrity even when undergoing structural changes. (f) Preservation of functional integrity despite structural loss could be interpreted as the age-related neurocompensatory mechanism. (g) In-silico studies have found that modulating biological parameters such as coupling strength and conduction delay may help to preserve functional integrity such as synchrony in the face of structural loss over age. Large-scale phase dynamical models such as the Kuramoto model have been used to connect structural decline and functional integrity in compensatory mechanisms. (h) Despite the research, the impact of short- and long-range connections on preserving functional integrity over age remains an open area of research. Scientists are still working to understand how changes in these connections impact the brain's overall functioning and ability to maintain cognitive health over time. (i) A large-scale dynamical model with the evolution of phase dynamics comprised of biophysical parameters such as global coupling strength and global conduction delay has been simulated to link the role of sub-graphs on the modulation of biophysical parameters in preserving functional integrity.

The white matter fibers that connect different regions and facilitate efficient communication between neurons undergo significant changes in terms of their length, strength, and myelination as a person ages [Sullivan and Pfefferbaum, 2006, Sullivan et al., 2010, Pannese, 2011], for illustration see Fig 1(b). Short-range connections (or local connections) are the most efficient communication pathways in the brain, as they allow for faster and more accurate transmission of information among closely connected regions [Mišić et al., 2015]. They reduce energy and resource consumption for forming, using, and maintaining brain connections, providing evolutionary benefits across species [Raichle and Mintun, 2006] (Fig. 1(c)). A previous study suggests that short-range white matter connections in the more anterior regions of the left hemisphere may continue to undergo myelination and axonal organization with age [Oyefiade et al., 2018]. Although the brain networks tend to prefer less costly short-range connections, they also have a small number of long (costly) connections, which may provide additional functionality [Avena-Koenigsberger et al., 2017]. The long-range connections (or distant connections) are essential for integrating information across different brain regions by reducing interareal distance [Sporns and Zwi, 2004] and for supporting more complex cognitive processes such as attention, memory, and decision-making [Bassett and Bullmore, 2006, Van Den Heuvel and Sporns, 2011, Ercsey-Ravasz et al., 2013, Bassett and Bullmore, 2017]. Betzel et al. showed that long-distance connections play a minor role in reducing topological distance in the brain, rather they contribute to functional diversity among brain areas, which leads to more complex brain dynamics [Betzel and Bassett, 2018]. Combining short- and long-range connections is essential for ensuring that information is transmitted quickly and efficiently across the brain and supporting a wide range of cognitive functions. A recent study shows that the strength and length of short-range and long-range connections in the brain may decline as we age [Petkoski et al., 2023]. Reduced cortical and subcortical long-range connectivity [Kana et al., 2011] and excess local connectivity is found in ASD [Dajani and Uddin, 2016].

There are several pieces of evidence from diverse fields, including neuroimaging, cognitive psychology, and neuropathology, supporting the notion that the aging brain is remarkably adaptable and resilient [Naik et al., 2017, Uddin, 2021, Aron et al., 2022] (the concept is placed in Fig. 1(d)). By retaining the ability to adjust and rebound, the aging brain preserves its functional efficiency at a desirable set point, known as functional integrity, which helps compensate for structural alterations [Marder and Goaillard, 2006, Betzel et al., 2014, Naik et al., 2017, Pathak et al., 2022, Petkoski et al., 2023]. There are several dynamical measures, such as neural synchrony, global metastability [Kelso, 2012, Deco and Kringelbach, 2016, Deco et al., 2017], derived from the instantaneous phase of resting state BOLD signals, which are better indicative of functional integrity [Deco et al., 2019] (see Fig. 1(e) for visual abstract).

The concept of neurocompensatory process in the face of anatomical decline along the aging trajectory is well explained and interpreted under the theoretical and biophysical backgrounds [Park and Reuter-Lorenz, 2009, Pathak et al., 2022, Petkoski et al., 2023] (Fig. 1(f)) and which happens through synaptic modifications, choosing alternative neural strategies and other adaptive mechanisms such as modulation of biological parameters (Fig. 1(g)). Petkoski et al. demonstrated that increased global coupling strength could compensate for structural loss during aging [Petkoski et al., 2023]. Evidence shows that some level of increased frontal activation with age can be a marker of an adaptive brain that engages in compensatory scaffolding in response to declining neural structures and functions [Park and Reuter-Lorenz, 2009]. Another recent study showed preservation in neural synchrony in aging through enhancing inter-areal coupling [Pathak et al., 2022]. The

biophysical mechanism is perfectly plausible from a mechanical viewpoint. However, it still needs to be understood which brain microcircuits contribute to the compensations and their role in calibrating the global scaling parameters, such as coupling strength and conduction delay, for overall structural connectivity loss with aging.

There is a fundamental knowledge gap regarding how the sub-graphs, connected via short- and long-range tracts, contribute to the compensatory mechanisms in the healthy aging process while preserving functional integrity. The work that we present has three related goals: (1) to identify sub-communities comprised of Short Range, Middle Range, and Long Range connections based on the white-matter tract lengths, (ii) to explore the dynamical effects of the two sub-graphs on different biophysical parameters associated with neuro compensation in aging, (iii) How the different biophysical parameters impacted by two sub-graphs when tested with mechanistic models captures changes in dynamics of the FC associated with aging. We try to fill this crucial gap (the workflow outlined in Fig. 1(h)) in the role of sub-graphs, parameters, compensation, and aging using the theoretical concepts and their biophysical interpretations.

We assume that the changes in the topology of structural connectivity in aging, together with the system parameters, control the emergence of collective or coordinated neural dynamics and age-associated variability in collective synchronization between brain areas ([Deco et al., 2017, Naik et al., 2017, Pathak et al., 2022, Petkoski et al., 2023]), evaluated under the measure of metastability as an indicative of functional integrity in healthy aging. The model allows us to mechanistically explore several hypotheses for the impact of demyelination on the propagation velocity and the existence of dynamic compensation for the lost connectivity. To this end, we perform in-silico tests using an anatomically constrained phase oscillator model (Kuramoto model [Kuramoto, 1984]) with coupling strength (k), which globally scale the local interaction strengths, and conduction delay (τ), which is associated with the local tract lengths and homogeneously scales the local delay to check the alterations in coordinated phase dynamics and observe how the system responds (in-terms of readjustment of parameters and emerged cortical coherence) when the structural topology alters. We justify the choice of this phase dynamical model by focusing only on the phase-dependent measure, i.e., metastability (Fig. 1(i)) as a key constraining factor in the age-related adaptive mechanisms. Structural changes associated with aging have been incorporated as the input to our model. We use the dynamical measure of metastability to evaluate functional integrity derived from the spatiotemporal evolution of phase dynamics of the empirical resting-state BOLD series obtained by fMRI and model simulations. The metastability captures the dynamical complexity or flexibility of the brain [Kelso, 2012, Deco et al., 2017]. It plays a crucial role in quantifying fluctuations in the instantaneous phase locking of resting-state BOLD signals [Naik et al., 2017], which indicates a healthy brain's ability to promptly react and respond to an internal or external stimulus. We systematically manipulate the empirical structural network of individual young subjects and simulate the large-scale generative model with personalized sub-graphs. We validated our findings using two completely independent cohorts consisting of 80 subjects from the CamCAN [Shafto et al., 2014, Taylor et al., 2017] repository and 39 subjects from the Berlin [Schirner et al., 2015] data sets, separated into two groups of young (18-34 years) and elderly (60-84 years) subjects. In neurodegenerative disorders such as multiple sclerosis, Alzheimer's, and Parkinson's, both short- and long-range connections in the brain are affected mainly over time [Ouyang et al., 2017, Meijer et al., 2020]. Our results suggest an avenue for using whole-brain models as a mechanistic tool to understand the role of short-range and long-range connections on crucial biophysical parameters to uncover the emergence of age-associated alterations in brain states. They

may provide an alternative pathway to treat age-related structural degeneracy, potentially supporting disease recovery.

2 Materials and Methods

We utilize two datasets for our study: one from the Cambridge Centre for Ageing and Neuroscience (CamCAN) cohort [Shafto et al., 2014,Taylor et al., 2017], and acquired at Berlin Center for Advanced Imaging, Charité University Medicine, Berlin, Germany [Schirner et al., 2015].

2.1 CamCAN dataset

2.1.1 Subjects

Our study includes 82 healthy participants (43 females and 39 males) from the Cambridge Centre for Ageing and Neuroscience (CamCAN) cohort. This cohort is available at http://www.mrc-cbu.cam.ac.uk/datasets/camcan/ and has been extensively described in previous studies [Shafto et al., 2014, Taylor et al., 2017]. We divided all participants into two groups: 41 young participants, ranging in age from 18 to 33 years (mean age = 25±4 years, 22 females), and 41 old participants, ranging in age from 60 to 86 years (mean age = 74±6.8 years, 21 females). We referred to these groups as 'YA' and 'OA,' respectively.

2.1.2 Data acquisition

Resting-state magnetic resonance imaging (MRI), including T1-weighted imaging, diffusion-weighted MRI, and functional MRI, was performed using a 3T Siemens TIM Trio scanner with a 32-channel head-coil at the Medical Research Council (UK) Cognition and Brain Sciences Unit (MRC-CBSU) in Cambridge, UK. High-resolution 3D T1-weighted data were acquired using a magnetization-prepared rapid gradient echo (MPRAGE) sequence with Generalized Autocalibrating Partially Parallel Acquisition (GRAPPA) acceleration factor of 2. Other acquisition parameters were as follows: repetition time (TR) = 2,250 ms, echo time (TE) = 2.99 ms, flip angle = 9°, field of view (FOV) = 256 × 240 × 192 mm; voxel size = 1 mm^3 isotropic, inversion time (TI) = 900 ms, and acquisition time (TA) = 4:32 min [Shafto et al., 2014]. Diffusion-weighted imaging data were collected using a twice-refocused spin echo sequence with a TR of 9100 ms, TE of 105 ms, FOV of 192 × 192 mm, isotropic voxel size of 2 mm^3, 66 axial slices using 30 directions with b = 1000 s/mm^2, 30 directions with b = 2000 s/mm^2, and three b = 0 images with a single average [Shafto et al., 2014]. For resting-state functional MRI, data with an EPI sequence were acquired with a TR of 1970 ms, TE of 30 ms, flip angle of 78°, FOV of 192 × 192 mm, voxel size of 3 × 3 × 4.44 mm^3, and 32 slices of thickness 3.7 mm, with participants' eyes closed during acquisition [Shafto et al., 2014].

2.1.3 DTI processing

The diffusion MRI data were processed locally using our pre-processing pipeline, which involved using MRtrix3 ([Tournier et al., 2019], https://github.com/MRtrix3/mrtrix3), FSL (http://www.fmrib.ox.ac.uk/fsl), and ANTS (http://stnava.github.io/ANTs/). The main preprocessing steps included denoising (using the MRtrix command 'dwidenoise', [Veraart et al., 2016]), removal of Gibbs ringing artifacts (using the MRtrix command 'mrdegibbs', [Kellner et al., 2016]), motion and eddy current corrections (using the MRtrix command 'dwifslpreproc', [Andersson et al., 2003]), and bias correction (using the MRtrix command 'dwibiascorrect' with ANTs, [Tustison et al., 2010]). Next, a brain mask was calculated in DTI space for each subject using the 'bet' command in FSL on the preprocessed image. To find the orientation of the fiber(s) (fiber orientation distribution, FOD) in each voxel, we used multi-shell multi-tissue constrained spherical deconvolution (MSMT-CSD; MRtrix command 'dwi2response' and 'dwi2fod', [Dhollander et al., 2018]). We then performed a global intensity normalization to make the fiber orientation distributions comparable between subjects. We used Anatomically Constrained Tractography (ACT, MRtrix command '5ttgen', [Smith et al., 2012]) to generate a tissue-segmented image. To use ACT, we preprocessed the T1-weighted image using MRtrix, then co-registered that image to the DWI using MRtrix and FSL. We created a mask of the gray matter/white matter boundary, which was helpful for streamline seeding. Finally, we used probabilistic tractography (MRtrix command 'tckgen') to generate 20 million tracts. The tractogram was further filtered (using the SIFT2 approach, MRtrix command 'tcksift2') to find a subset of streamlines such that the streamline densities were closer to fiber densities [Smith et al., 2015]. Each step was visually assessed and edited by research personnel.

2.1.4 T1 processing

From, Freesurefer http://surfer.nmr.mgh.harvard.edu [Dale et al., 1999], 'recon-all' was employed to reconstruct a two-dimensional cortical surface from a three-dimensional volume acquired from T1-weighted image. The steps involved skull stripping from the anatomical image, estimation of interface between the white matter and grey matte, and generation of white and pial surfaces. The Desikan-Killiany atlas [Desikan et al., 2006] with 68 regions of interest (ROIs) was used for cortical parcellation.

2.1.5 Structural connectivity and fiber tract length

A whole-brain connectome was generated for each subject based on the Desikan–Killiany atlas by computing the fiber density between every pair of regions of interest (ROIs) using the MRtrix command 'tck2connectome' with the option 'scale_invnodevol.' This allowed us to quantify the number of streamlines originating from one ROI and reaching each of the other ROIs. The physical length of the fiber was calculated in millimeters between each pair of ROIs, with a maximum tract length of 250 mm. A tract length (TL) matrix was generated for each subject based on the Desikan–Killiany parcellation.

2.1.6 fMRI preprocessing

Resting-state functional MRI (fMRI) for individual subjects was pre-processed using the CONN toolbox [Whitfield-Gabrieli and Nieto-Castanon, 2012] (https://web.conn-toolbox.org/), which is a Matlab/SPM-based software. The data were pre-processed using the default CONN pipeline with a TR of 1.9 sec. The pre-processing steps included unwrapping using field-map images, realignment to correct for motion, slice timing correction, segmentation, normalization to the MNI template, outlier rejection, and functional smoothing. Spatial smoothing was performed using a Gaussian kernel with a full width of 6.0 mm. Denoising was performed to remove signal changes related to white matter, cerebrospinal fluid, motion, breathing, and cardiac pulsations. Finally, temporal band-pass filtering (0.04-0.9 Hz) and linear detrending were applied. For region of interest (ROI) analysis, the mean regional BOLD time series were estimated in 68 parcellated brain regions of the Desikan–Killiany atlas [Desikan et al., 2006].

2.1.7 Empirical functional connectivity

Aggregated BOLD time series of each region were z-transformed, and then pairwise Pearson correlation coefficients were computed to obtain 68×68 resting state functional connectivity (rsFC) matrix for individual subjects.

2.2 Berlin dataset

2.2.1 Subjects

In this study, we also analyze another dataset by Charité University Berlin in [Schirner et al., 2015]. Forty-nine healthy subjects (30 females and 19 males) participated after providing written informed consent to Charité University Berlin [Schirner et al., 2015]. The experiments were conducted under the relevant laws and institutional guidelines and approved by the ethics committee of Charité University Berlin [Schirner et al., 2015]. The age of the subjects ranged from 18 to 80 years, with a mean and standard deviation of 41.55±18.44. We divided the subjects into two groups: 26 young participants aged 18 to 33 years (mean=25.7±4 years; 13 female) and 14 elderly participants aged 57 to 80 years (mean=70.99±9 years; 8 female). An automated pipeline was proposed [Schirner et al., 2015] for constructing individualized virtual brains, and the pipeline comprised several state-of-the-art neuroinformatics tools to generate subject-specific cortical and subcortical parcellations, surface-tessellations, structural and functional connectomes, lead field matrices, electrical source activity estimates, and region-wise aggregated BOLD fMRI time-series [Schirner et al., 2015].

2.2.2 Empirical structural connectivity, tract length, functional connectivity

T1 structural magnetic resonance images (MRI), diffusion-weighted images (DWI), and functional MRI were acquired at the Berlin Center for Advanced Imaging, Charité University Medicine, Berlin, Germany, using a 3T Siemens Trim Trio scanner and a 12-channel Siemens head coil. The voxel size was specified, and the data acquisition tools and pre-processing steps were described in Schirner et al. [Schirner et al., 2015]. Cortical grey matter parcellation was performed using the

Desikan-Killiany parcellation method [Desikan et al., 2006], resulting in 34 regions of interest (ROIs) in each hemisphere. Tractography was constrained by seed, target, and stop masks, and the fiber length was represented in millimeters.

The same participants underwent a functional MRI scan during which their eyes-closed, awake, resting-state data were acquired for 22 minutes (repetition time, TR=2 sec). Each region's pre-processed BOLD time series were z-transformed, and pairwise Pearson correlation coefficients were computed to obtain each subject's resting-state functional connectivity (rs-FC) matrix. All experiments were conducted under the relevant laws and institutional guidelines, and the Charité University Berlin ethics committee approved them.

Table 1: Demographic data of two age groups in two datasets.

Dataset	YA Total(Female)/mean age±sd	OA Total(Female)/mean age±sd
Cam-CAN (n=82)	Age range 18-33 41(22) / 25 ± 4	Age range 60-86 41(21) / 74 ± 6.8
Berlin (n=40)	Age range 18-33 26(13) / 25.68 ± 4	Age range 57-80 14(8) / 70.99 ± 9

2.3 Defining connectivity based on fiber lengths: SR, MR and LR

There are several definitions available in the existing literature to define short-range (SR), middle-range (MR), and long-range (LR) connections between two ROIs [Wu et al., 2014, Meijer et al., 2020]. Generally, SR connections are intra-regional connections, including intracortical and subcortical connections. MR tracts connect spatially close but distinct regions, including association tracts, commissures, and cortical-subcortical pathways. LR fibers connect spatially distant areas, including inter-hemispheric, cortico-cortical, and cortical-subcortical pathways.

In this study, we defined short, middle, and long-range connections based on fiber tract length setting two thresholds, one at 70 mm and another at 140 mm for CamCAN, and 56mm and 130mm for Berlin, see Table 2. The choice of threshold was based on the approximation of the first (the lower threshold for SR) [Meijer et al., 2020] and third (the upper threshold for LR) quartiles of the average tract length distribution among young subjects. In Fig. 2(a), we plotted the average fiber tract lengths of the young group. We based our choice of threshold on the approximate first (lower threshold) and third (upper threshold) quartiles of the average tract length distribution. The two blue vertical lines in Fig. 2(a) indicate the lower threshold (e.g., 70mm) and upper threshold (e.g., 140mm) for SR and LR, respectively.

Table 2: Defining SR, MR, and LR connections for the CamCAN and Berlin datasets.

	SR tracts	MR tracts	LR tracts
CamCAN dataset	tract length $\leq$ 70 mm	70 mm $<$ tract length $<$ 140 mm	140 mm $\leq$ tract length
Berlin dataset	tract length $\leq$ 56 mm	56 mm $<$ tract length $<$ 130 mm	130 mm $\leq$ tract length

2.4 Defining sub-communities comprised of SR, MR, and LR connections

The sub-communities are defined based on their connection types and combinations, as follows:

(i) Sub-community comprised of SR and MR connections without LR connectivity is denoted as Y_{SR+MR}. We keep

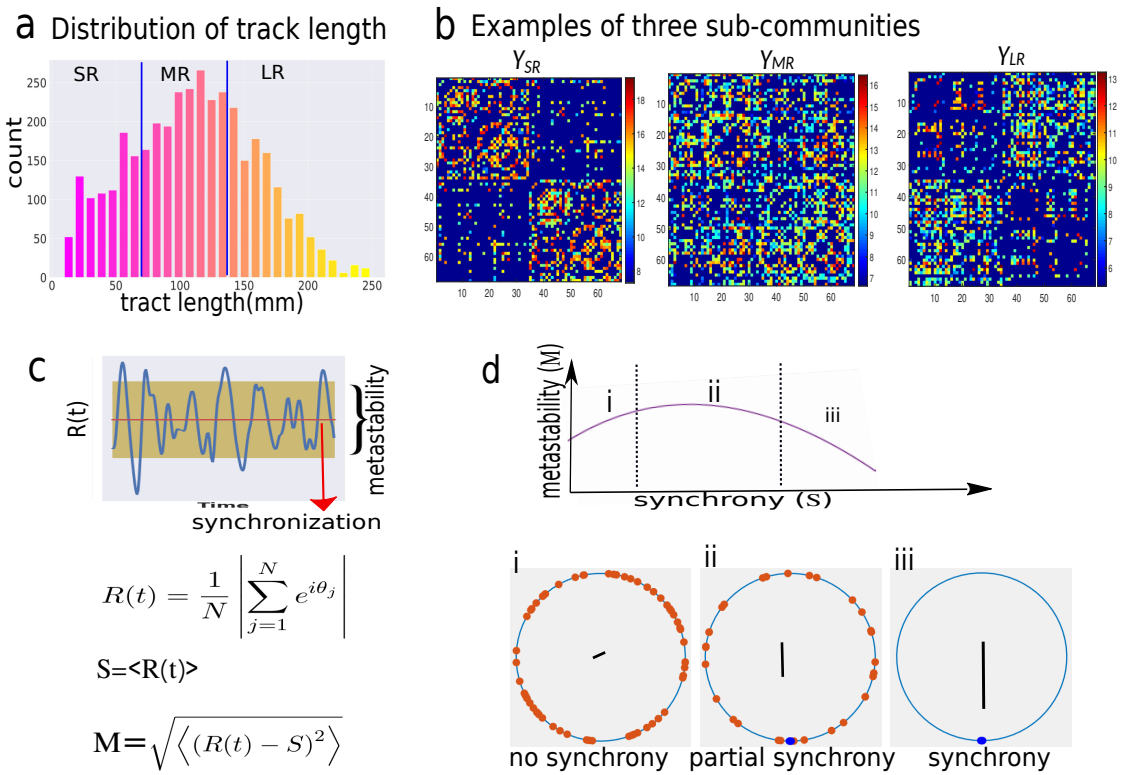

Figure 2: **Overview of anatomy and function analysis**. (a) The graph shows the average tract length distribution among young subjects of the CamCAN dataset, where the blue vertical lines represent the lower (70mm) and upper (140mm) thresholds. The lengths are categorized into short-range (SR), middle-range (MR), and long-range (LR) based on the thresholds. (b) The intact structural connectivity is separated according to the SR, MR, and LR categories. (c) The Kuramoto order parameter ($R(t)$) is plotted against time, where the red line represents the mean of $R(t)$ that quantifies global synchrony (S). The yellow confidence interval indicates fluctuations in $R(t)$, defined as metastability (M). The analytical expressions of the two dynamical measures are provided below the temporal plot. (d) The relationship between synchrony and metastability is shown in the right panel, which follows a non-linear relationship. The metastability is maximum when the system is partially synchronized. In correspondence to the M-S characteristic curve, the coherence status is shown for (i) de-synchrony, (ii) partial synchrony, and (iii) in-phase synchrony states by the three color-coded phase circle diagrams.

SR and MR fibers and removed LR connections from the young adult's structural connectivity (SC), tract length, and functional connectivity (FC).

(ii) Sub-community containing only SR tracts, without LR and MR fibers, is labeled as Y_{SR}.

(iii) Sub-community, labeled as Y_{MR+LR}, connected via MR and LR connections without SR. We retain MR and LR connections while removing all SR connections from the young adults.

(iv) Y_{LR} is the sub-community connected only via LR connections without SR and MR tracts from individual young participants.

An example of three sub-communities generated from a young subject, based on the tract length distribution [Fig. 2(a)], is shown in Fig. 2(b), where the subscripts represent the type of sub-community. Based on the connection types, three exemplary sub-communities are derived from the structural connectivity of young individuals shown in Fig. 2(b). The sub-community connected via SR tracts is solely derived from the young SCs, labeled as Y_{SR}, and defined as the SR sub-community of anatomical counts between a given pair of regions. Y_{MR}, is comprised of MR connections only between any pair of regions, shown in Fig. 2(b), middle column. The LR sub-community derived from young SCs is denoted as

Y_{LR} and defined as the sub-community comprised of long-range tracts only, shown in Fig. 2(b), third column.

2.5 Graph theoretical metrics

The network properties were computed using BCT [Rubinov and Sporns, 2010]. We consider two weighted graph metrics: the mean (mean-FC) and variance (var-FC) of the FC matrix. Each is calculated by finding the corresponding statistic (mean and variance) of the upper triangular portion of the FC matrix, excluding the diagonal. We considered five unweighted graph metrics: modularity, clustering coefficient, assortativity, global efficiency, and characteristic path length. The brain network's segregation is captured by measuring the modularity and clustering coefficients. The integrative capabilities of a network can be captured by global efficiency and characteristic path length. The definition and description of the graph theoretical metrics are:

(i) Modularity [Newman, 2006], $M = \frac{1}{l}\sum_{(i,j\in N)}\left[w_{ij} - \frac{k_i k_j}{l}\right]\delta_{m_i m_j}$, where l is the sum of weights in the network; w_{ij} is the connectivity weight between nodes i and j; k_i, k_j are the weighted degrees of nodes i and j, respectively. Modularity gives network resilience and adaptability, measuring the degree of segregation. Communities are subgroups of densely interconnected nodes sparsely connected with the rest of the network. In the case of a functional network, modularity signifies coherent clusters of functional modules.

(ii) Clustering coefficient :The clustering coefficient for a single node is the average relative number of triangles around a node. For adjacency matrix A, the nodal clustering coefficient for node i is $\frac{1}{\sum A_{ij}(\sum A_{ij}-1)}\sum_{j,k,j\neq k} A_{ij}A_{jk}A_{ik}$. The clustering coefficient for the network is the average of the nodal clustering coefficients.

(iii) Assortativity [Newman et al., 2006], $A = \frac{l^{-1}\sum_{(i,j\in L)} w_{ij}k_i k_j - \left[l^{-1}\sum_{(i,j\in L)}\frac{1}{2}w_{ij}(k_i+k_j)\right]^2}{\left[l^{-1}\sum_{(i,j\in L)}\frac{1}{2}w_{ij}\left(k_i^2+k_j^2\right)\right]-\left[l^{-1}\sum_{(i,j\in L)}\frac{1}{2}w_{ij}(k_i+k_j)\right]^2}$, where k_i, k_j are the weighted degrees of nodes i and j, respectively; w_{ij} is the connectivity weight between nodes i and j; L is the set of all edges within the network, and l is the total number of edges. Functional network resilience is assessed utilizing the assortativity [Newman, 2003, Newman, 2002].

(iv) Global efficiency [Latora and Marchiori, 2001], $E = \frac{1}{n}\sum_{i\in N}\frac{\sum_{j\in N, j\neq i} d_{ij}^{-1}}{n-1}$, where N is the set of all nodes; n is the total number of nodes; d_{ij} is the weighted shortest path length between node i and j. It captures the integration property of a network.

(v) Characteristic path length [Watts and Strogatz, 1998], $L = \frac{1}{n}\sum_{i\in N}\frac{\sum_{j\in N, j\neq i} d_{ij}}{n-1}$, where N is the set of all nodes; n is the total nodes; d_{ij} is the weighted shortest path length between i and j.

2.6 Large-scale generative model: Kuramoto model phase dynamics

We selected the Kuramoto model to capture phase transition and global synchrony status with anatomical parameters. The model provides tractable network dynamical measures of whole-brain synchrony and metastability and can capture the key qualitative features of complex brain dynamics. We modeled the dynamical interactions between each N (=68) node as a phase oscillator, spatially coupled via structural connectivity [Kuramoto, 1984, Cabral et al., 2011, Breakspear

et al., 2010]. The Kuramoto model incorporates two biophysical parameters: conduction delay (τ) and global coupling strength (κ). Two underlying assumptions are made, i.e., local neural activity is periodic, and the coupling between local neural populations is weak enough to neglect amplitude effects [Daffertshofer and van Wijk, 2011]. The anatomically constrained phase model is computationally less intensive and can simulate microscopic neural dynamics related to underlying structural connectivity [Shanahan, 2010, Cabral et al., 2011, Hellyer et al., 2014, Messé et al., 2014] and emerged collective phase dynamical states.

The dynamics of the ith phase oscillator (i.e., a brain area) is governed by the Kuramoto phase oscillators as,

$$\frac{d\theta_i}{dt} = \omega_i + \kappa \sum_{j=1}^{N} C_{ij} \sin\left[\theta_j(t - \tau \frac{L_{ij}}{\langle L_{ij} \rangle}) - \theta_i(t)\right], \tag{1}$$

where $i, j = 1, 2, \cdots N$. $N(=68)$ is the total number of brain regions or the network size. C_{ij}, the normalized connection weights between the ith and j^{th} node. θ_i is the phase of ith oscillator, where ω_i is the intrinsic frequency of oscillation. κ is the global coupling coefficient that scales local connection strengths between regions. τ_{ij} is the conduction delay between node i and j, defined as τ_{ij}=L_{ij}/v, i.e., the ratio of the fiber distance (L_{ij}) and mean conduction speed (v) of current through the fibers. For simplicity, we consider the mean conduction delay τ, as $\langle \tau \rangle = \langle L \rangle / v$, where $\langle L_{i,j} \rangle$ is the average fiber length. The mean delay can also be interpreted as the global scaling parameters for the local delay between regions. To simplify the model, we assume that the nodes behave as homogeneous neural masses in which all neurons oscillate together. Each node oscillates freely at a fixed frequency of ω_i=ω=$2\pi \times 60$ Hz. The model has two free parameters, κ, and τ. We perform parameter space sweeps to characterize the network dynamics for the entire relevant parameter range. Initial values of the phases are drawn from a normal distribution for a range of $\theta_i(0) \in (-\pi, \pi)$. We simulate the phase model for a total interval of 80 seconds, where the first 10 seconds of transients are discarded. Numerical integration of the coupled system was performed using the Euler method with a time step of Δt=0.1 ms. All numerical simulations are performed in MATLAB 2021b (MathWorks). BrainNet Viewer is used for glass brain plots. Python is used to plot other figures.

To correlate the simulated neural activity with the empirically recorded BOLD activity from the subjects, we converted the former to the latter. The fluctuations in firing rate for node n, denoted as $r_n(t)$, fluctuate around a fixed value and are obtained by a periodic function of the local node phase [Cabral et al., 2011]. We chose a simple sine function for these fluctuations, defined as $r_i(t) = r_0 \sin(\theta_i(t))$, where the amplitude is kept at r_0=1. Next, we used the Balloon-Windkessel hemodynamic model to convert the neural signal to model-based BOLD activity, following methods described in [Cabral et al., 2011].

2.7 Dynamical measure: metastability

We derive metastability for both empirical and computational BOLD signals. The empirical and model-based BOLD signals are converted into a complex phase representation (analytic signal). We compute the analytic signal (y_j) from the

BOLD series of jth brain region as,

$$y_j(t) = x_j(t) + iH(x_j(t)) = r(t)e^{i\theta_j(t)},$$

where $H(x_j(t))$ represents Hilbert transform of the original signal $x_j(t)$. The instantaneous amplitude and phase of the corresponding BOLD signal are $r(t)$ and $\theta_j(t)$. A pictorial representation of synchrony and metastability with their definitions is shown in Fig. 2(c).

The Kuramoto order parameter [Kuramoto, 1984], $R(t)$ is defined as,

$$R(t) = \frac{1}{N}\left|\sum_{j=1}^{N} e^{i\theta_j(t)}\right|.$$

The value of $R(t)$ quantifies the global coherence status of the network at time t, ranging from $0 \leq R(t) \leq 1$, where 0 implies no synchrony [Fig. 2(d)i] and 1 indicates complete or in-phase synchrony state [Fig. 2(d)iii], otherwise partially synchronized [Fig. 2(d)ii]. Mean phase synchrony captures the global coherence status in the network and is defined as,

$$S = \frac{1}{T}\sum_{t=1}^{T} R(t) = \frac{1}{T}\sum_{t=1}^{T}\frac{1}{N}\left|\sum_{j=1}^{N} e^{i\theta_j}\right|,$$

where N represents the total number of regions (nodes).

Metastability captures the fluctuations in the synchrony states and is defined as the standard deviation of order parameters over time. The correlation between synchrony and metastability is shown in Fig. 2(d).

$$Metastability = \mathcal{M} = \sqrt{\left\langle (R(t) - S)^2 \right\rangle}$$

where, $\langle . \rangle$ indicates the time average.

In the model simulation, we choose a range of 0.1 to 50 for κ and τ with an increment interval of 0.6 to capture the metastability map on the τ-κ parameter plane. The model is simulated to generate the metastability map for each pair of τ and κ for individual subjects, further utilized to estimate the optimal τ and κ parameters.

2.8 Model-based parameter estimation: optimal coupling strength (κ) and delay (τ)

We utilized a computational framework employing a large-scale brain network model to investigate optimal brain function during a state of maximum metastability at rest [Deco et al., 2017,Surampudi et al., 2019]. The hypothesis of a maximum metastable state is associated with optimal information processing capability and switching behavior of the brain [Deco and Kringelbach, 2016, Deco et al., 2019]. We utilized the maximum metastability condition to compare the degrees of metastability on the two-parameter plane as a critical constraint to estimate the parameters, κ^{opt} and τ^{opt}. (I) We determined the optimal coupling strength (κ) and delay (τ) values from the metastability map at the level of the individual subject. We compute $\mathcal{M}(\kappa, \tau)$ for each value of the two parameters to generate a two-parameter space. Next,

we determine the optimal parameters utilizing a condition as :

$$[\kappa, \tau]^{opt} = argmax(\mathcal{M}(\kappa, \tau)).$$

(II) The optimal values of κ and τ were determined at the individual subject level. The obtained optimal values were subjected to statistical tests to compare young and older age groups.

2.9 Group level comparison: statistical measures

We conducted independent t-tests, using MATLAB built-in function $ttest2$, to compare group differences between young and elderly subjects in the case of the CamCAN dataset and the Mann-Whitney U-test for Berlin data. All statistical analyses were performed using MATLAB, and all reported significance levels are two-sided, with a significance level of $p < 0.05$.

3 Results

3.1 White matter fiber length and count

We classify the SR, MR, and LR connections using a lower threshold of 70 mm for CamCAN and 56 mm for Berlin and an upper threshold of 140 mm for CamCAN and 130 mm for Berlin. This enabled us to identify the sub-graphs connected via SR, MR, and LR connections. The average tract length distribution of young and elderly subjects for CamCAN and Berlin cohorts is presented in Figs. 3(a) and 3(d), respectively. On average, there is a reduction of 13% in tract length for CamCAN and 2% for Berlin in the elderly population, which could be due to volume shrinkage [Peters, 2006] or fiber dissociation with age, tabulated in Table 3 for the entire network and other sub-graphs. Figures. 3(b) and 3(e) show scatter plots of subject-wise tract lengths of SR, MR, and LR arranged from left to right panels for CamCAN and Berlin data, respectively. The black lines in Fig.3(b) represent the standard deviations from each group's mean values of tract lengths. The dashed blue lines connect the mean values of the two groups and exhibit a decaying pattern in tract lengths for elderly subjects. The blue and red dots in the plot corresponds to the group's YA and OA, respectively. The double stars (**) in Fig.3(b) and the single star (*) in Fig.3(e) indicate statistical significance with $p<10^{-6}$ and $p<0.05$, respectively. We estimate the percentage of decay in tract lengths for elderly subjects in the CamCAN dataset as 6%, 2%, and 3% and for the Berlin dataset as 3%, 2%, and 0.1% for SR, MR, and LR, respectively (see Table 3).

Next, we examine the reduction in the total number of tracts (counts or strengths). Figures. 3(c) and 3(f) display the violin plots of fiber strengths in the first panel for the CamCAN and Berlin datasets, respectively. Blue and red violins for the YA and OA, respectively. A significant decrease in the total fiber counts is observed in elderly subjects.

Total counts of SR, MR, and LR tracts for young and old subjects are shown in Fig. 3(e) in the CamCAN) and Fig. 3(f) for Berlin datasets. Table 3 tabulates the mean (standard deviation), t-statistic, p-value, percentage of change in fiber

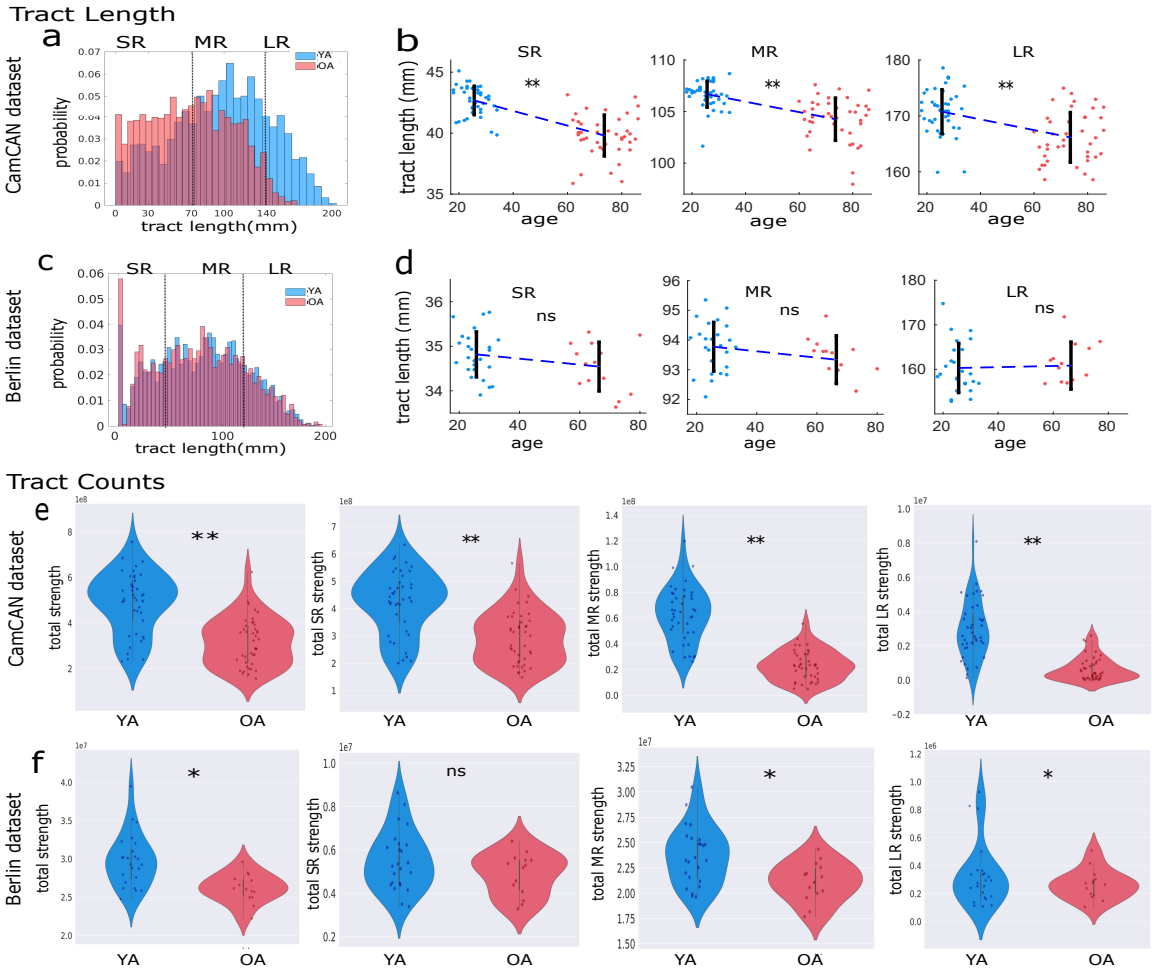

Figure 3: Results from anatomical data analysis shown in (a,b,e) for CamCAN and (c,d,f) Berlin data. (a,c) Distribution of average tract lengths of YA and OA cohorts. (b,d) Distribution of tract lengths (mm) for three sub-communities for YA and OA. (e,f) Distribution of total fiber tract counts of short-range (SR), middle-range (MR), and long-range (LR) connections for the two aging cohorts. Blue and red colors represent YA and OA, respectively.

length, and fiber strength (count) for the young and old groups. The results show a significant reduction in fiber length and fiber strength (count) in the brains of elderly individuals when compared to their younger counterparts across the entire network and all types of sub-graphs.

SR connections largely dominate the strength of connections in the brain, with approximately 84% of the total connection strength for CamCAN and 78% for Berlin. On average, there is a reduction of approximately 31% in SR tract strength for CamCAN and approximately 4% for Berlin in elderly subjects. In contrast, LR connection strength has minimal overall strength, accounting for only 0.6% for CamCAN and 0.7% for Berlin. However, in the elderly group, LR connection strength is found to have deteriorated significantly, with a reduction of 78% for CamCAN and 5% for Berlin.

3.2 Functional connectivity reorganization

Graph theory have provided many new methods for topologically analysing brain networks, some of which have already been translated to the characterization of functional brain networks [Bullmore and Sporns, 2009]. Here, we measure the statistical and topological properties of the functional connections. At first, empirical resting state functional connectivity

(rsFC) is constructed using pairwise Pearson correlations between any two given areas' BOLD signals. We convert the original FC matrix into a binary graph by applying a threshold on the absolute values of edge weights (correlation coefficients corresponding to p<0.05). Thus, the FCs are converted into a binary network by setting the condition as $FC_{i,j}$=1, if abs($FC_{i,j}$) $> \delta$, where δ=0.12; otherwise, $FC_{i,j}$=0. Threshold correlation coefficient corresponding to significant functional connections with p-values <0.05 (i.e., abs(FC) $\geq$ 0.12. Additionally, we ensure that this process does not result in nodes becoming isolated or disconnected from the network. This binarised network construction is essential for capturing the most influential connections while preserving the overall functional graph topology [Shinn et al., 2023]. To understand the functional network characteristics comprehensively, we employ various graph metrics, such as modularity, mean clustering coefficient, assortativity, global efficiency, and characteristic path length. In addition to these metrics, we consider weighted measures capturing statistical dependencies, such as, the mean and variance of the weighted functional connectivity. These weighted measures provide insights into the strength and variability of connections within the network. Figure 4(a, b) shows various network metrics for two cohorts (CamCAN and Berlin). Table 3 presents detailed results for measures in both age groups and two datasets. We observe significant FC mean and variance alterations when comparing older adults (OA) to younger adults (YA). This indicates substantial changes in the strength and variability of functional connections with aging. Additionally, there is a significant increase in global efficiency and a reduction in modularity, while assortativity was preserved in older adults compared to younger adults. These findings collectively demonstrate functional reorganization in aging, highlighting nuanced changes in network properties and shedding light on the intricate dynamics of the aging brain.

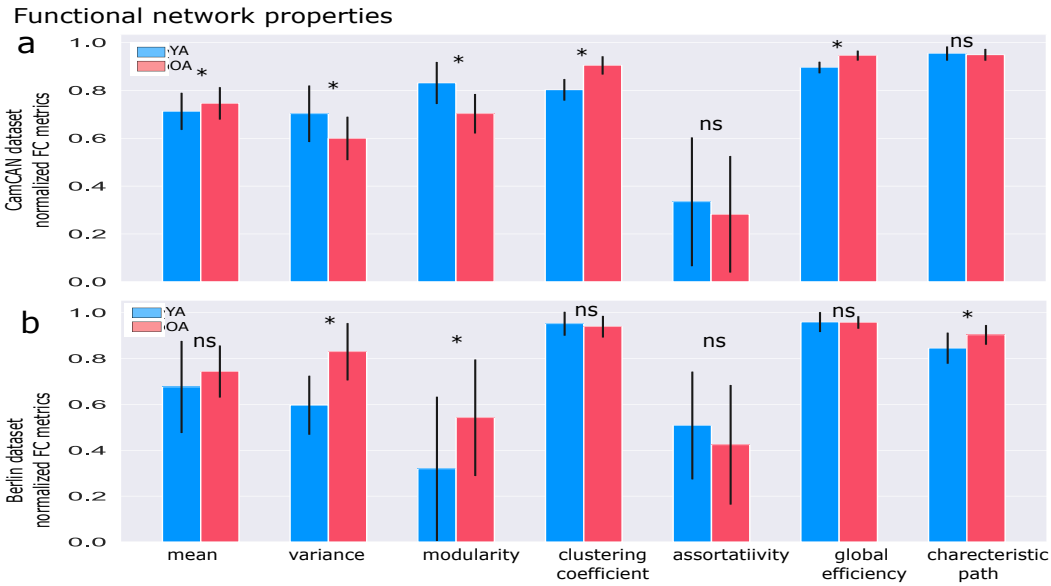

Figure 4: Empirical rsFC analyses are performed for two datasets: (a) CamCAN and (b) Berlin data. Blue and red colors are used to represent Young Adults (YA) and Older Adults (OA), respectively. The star ($*$) indicates statistical significance, p<0.05. The ns denotes non-significant changes. Comparisons between the two age groups indicate alterations in statistical properties of the FCs but remain topologically invariant.

3.3 Empirical resting state brain dynamics

We assess the metastability of large-scale neural dynamics in young and old subjects, measured using 68 regional phase time courses derived from resting-state fMRI BOLD data in both groups. Figure 5(a, b) shows the empirical metastability over two cohorts. Our findings reveal no statistically significant difference in metastability between the young and older adults for CamCAN and Berlin datasets. The results suggest that at the level of large-scale neural dynamics, the overall stability or variability in brain dynamical repertoire appears invariant in both groups. In other words, despite the potential age-related changes in brain structure and function, the fundamental aspect of the brain's dynamic complexity at a slow time scale appears to remain relatively consistent.

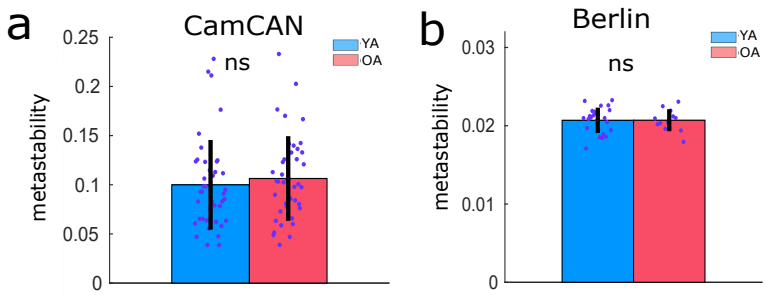

Figure 5: Brain's dynamical complexity quantified by the metastability measure from resting state fMRI BOLD signals of YA and OA for (a) CamCAN and (b) Berlin cohorts. Blue and red color represent YA and OA, respectively. *ns* indicates no significant changes between the groups, i.e., $p>0.05$. The consistent level of metastability implies sustained brain dynamics at rest in the two aging cohorts.

Table 3: Mean (SD) fiber length and fiber strength (count) for the entire network and three sub-graphs, as well as functional network properties for both groups. The percentage of reduction is calculated as the percentage of relative changes in fiber parameters from YA to OA.

	YA mean(sd)	OA mean(sd)	Statistics	Percentage of reduction
CamCAN dataset			(t-test)	
Entire network tract length (mm)	113 (7.2)	98 (8)	-7.85 **	13%
SR tract length (mm)	43 (1.2)	40 (1.7)	-8.89 **	6%
MR tract length (mm)	107 (1.2)	105 (2.0)	-6.37 **	2%
LR tract length (mm)	171 (3.1)	166 (4.1)	-4.91 **	3%
Entire network fiber strength (counts)	5.1×10^8 (1.3×10^8)	3×10^8 (1.05×10^8)	-6.54 **	35 %
SR fiber strength (counts)	4.3×10^8 (1×10^8)	3×10^8 (0.09×10^8)	-5.71 **	31%
MR fiber strength (counts)	0.54×10^8 (0.2×10^8)	0.2×10^8 (0.1×10^8)	-10.51 **	64%
LR fiber strength (counts)	0.03×10^8 (0.01×10^8)	0.007×10^8 (0.007×10^8)	-8.19 **	78%
FC Mean (weighted network)	0.72 (0.07)	0.74 (0.06)	-2.40 *	-
FC Variance (weighted network)	0.70 (0.10)	0.59 (0.10)	5.09*	-
FC Modularity	0.84 (0.10)	0.72 (0.09)	9.06 ^{ns}	-
FC Clustering coefficient	0.80 (0.04)	0.90 (0.03)	-12.76^{ns}	-
FC Assortativity	0.33 (0.20)	0.28 (0.24)	01.06 ^{ns}	-
FC Global efficiency	0.90 (0.03)	0.95 (0.02)	2.03*	-
FC Characteristic Path length	0.95 (0.02)	0.94 (0.02)	1.00^{ns}	-
Berlin dataset			(U test)	
Entire network tract length (mm)	100 (7.1)	98 (4.8)	0.27 ^{ns}	2%
SR tract length (mm)	35 (0.5)	34 (0.5)	1.21 ^{ns}	3%
MR tract length (mm)	94 (0.82)	93 (0.8)	1.53 ^{ns}	1%
LR tract length (mm)	160 (5.1)	159 (5.6)	0.29 ^{ns}	0.1%
Entire network fiber strength (counts)	2.9×10^7 (0.3×10^7)	2.6×10^7 (0.2×10^7)	-3.03 *	11%
SR fiber strength (counts)	2.2×10^7 (0.2×10^7)	2.1×10^7 (0.2×10^7)	-1.21 ^{ns}	4%
MR fiber strength (counts)	0.72×10^7 (0.2×10^7)	0.5×10^7 (0.1×10^7)	-3.39 *	3%
LR fiber strength (counts)	0.02×10^7 (0.2×10^7)	0.01×10^7 (0.1×10^7)	-2.09 *	5%
FC Mean (weighted network)	0.68 (0.20)	0.65 (0.10)	123^{ns}	-
FC Variance (weighted network)	0.59 (0.12)	0.77 (0.11)	29 *	-
FC Modularity	0.32 (0.06)	0.55 (0.25)	73 *	-
FC Clustering coefficient	0.95 (0.05)	0.86 (0.20)	171 ^{ns}	-
FC Assortative	0.51 (0.22)	0.42 (0.20)	175.5 ^{ns}	-
FC Global efficiency	0.96 (0.04)	0.96 (0.02)	168^{ns}	-
FC Characteristic Path length	0.84 (0.12)	0.90 (0.04)	62 *	-

3.4 Model-based synchrony and metastability for three sub-graphs

Our primary analysis focuses on the role of short-range (SR) and long-range (LR) connections in maintaining functional integrity in the brain. However, medium-range (MR) connections may also be crucial for the global dynamical behavior of SR and LR connections. Therefore, investigating the functional role of SR and LR connections in conjunction with MR connections could lead to more robust and comprehensive findings. To this end, we create four distinct sub-communities by selectively deleting targeted links from the healthy young's anatomical connectivity for further analysis. These sub-communities are defined based on their connection types and combinations, as follows:

(i) Sub-community comprised of SR and MR connections without LR connectivity is denoted as Y_{SR+MR}. We keep SR and MR fibers and removed LR connections from the young adult's structural connectivity (SC), tract length, and functional connectivity (FC).

(ii) The sub-community containing only SR tracts, without LR and MR fibers, is labeled as Y_{SR}.

(iii) The sub-graph, labeled as Y_{MR+LR}, connected via MR and LR connections without SR. We retain MR and LR connections while removing all SR connections from the young adults.

(iv) Y_{LR} is the sub-graph connected only via LR connections without SR and MR tracts from individual young participants.

Subsequently, we simulate the personalized generative model with the four sub-graphs and intact young and older adults' structural connectivity. We vary κ and τ to generate synchrony and metastability maps for individual subjects. We then compare the estimated results of young adults to those of older adults.

Figure 6(a) displays the whole networks of young adults (YA), older adults (OA), and other sub-graphs, including those with both short-range and mid-range connections (Y_{SR+MR}), only short-range connections (Y_{SR}), both mid-range and long-range connections (Y_{MR+LR}), and only long-range connections (Y_{LR}). Figure 6(b) illustrates the synchronization (first row) and metastability map (second row) on τ-κ parameter space for YA, OA, and other four sub-graphs. The region of maximum metastability (depicted in dark red in Fig. 6)) extends in the positive direction of the coupling strength for OA compared to YA. However, the value of maximum metastability (see color bar) remains the same for both groups, indicating modulation of the global coupling strength while achieving maximal metastability.

To further assess the similarity between the simulated metastability patterns of OA and the sub-graphs, we average the corresponding maps of each subject and then calculate the pairwise Pearson correlation coefficient between the metastability maps of OA and Y_{SR+MR}, OA and Y_{SR}, OA and Y_{MR+LR}, and OA and Y_{LR}. The correlation values are presented in Table 4. The high correlation values observed between the metastability heat-maps of young adults (YA) and

Table 4: Correlation between the average metastability maps of OA and the corresponding maps of YA, Y_{SR+MR}, Y_{SR}, Y_{MR+LR}, and Y_{LR} for the CamCAN and Berlin dataset.

	YA	Y_{SR+MR}	Y_{SR}	Y_{MR+LR}	Y_{LR}
CamCAN dataset	0.90	0.80	0.78	0.36	0.46
Berlin dataset	0.95	0.93	0.76	0.70	0.56

older adults (OA) indicate that the synthetic metastability patterns remain similar between the two age groups, further supporting our observation on metastability derived from empirical data. To identify which sub-graphs exhibit more similarity in patterns with the OA group, we compared the metastability maps of OA with those of defined networks.

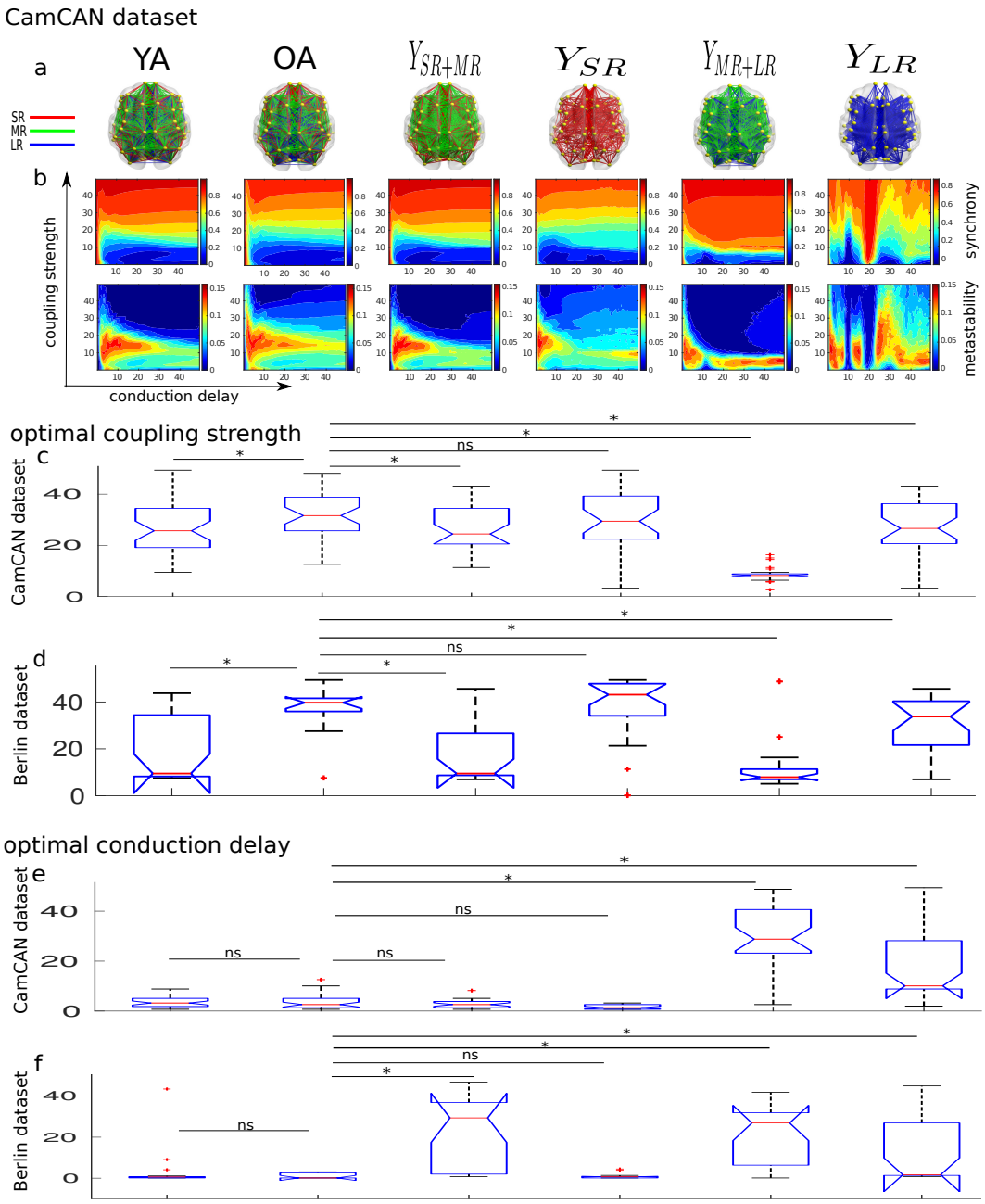

Figure 6: **Effects of short-range (SR), middle-range (MR), and long-range (LR) connections on global brain dynamics based on data from CamCAN and Berlin.** Top panel (a) shows schematic brain views of average tracts for various sub-graphs, including young adults (YA), older adults (OA), and sub-groups with varying combinations of SR, MR, and LR connectivity. Plots for the synchronization and metastability heatmaps, optimal coupling strengths, and conduction delays are placed below each sub-group. The second panel (b) displays synchronization and metastability maps for each of the six cases, generated by taking the average over subjects. Panels (c) and (d) show box plots of model-based optimal coupling strengths estimated from individual subjects. We observe significant modulation in coupling strength in OA subjects compared to YA and significant changes between OA and the cases of Y_{SR+MR}, Y_{MR+LR} and Y_{LR}, but not with Y_{SR}. Panels (e) and (f) display optimal conduction delay estimates for each case at the individual subject level. We find modulation in delay parameter in cases of Y_{SR+MR}, Y_{MR+LR}, and Y_{LR}, indicating a significant influence of LR on the delay. The non-significant change in OA compared to YA might be due to the absence of LR connections in elderly subjects, thus having no impact of LR on delay in the elderly. Overall, our analysis comparing OA and Y_{SR} showed no significant changes in the target levels of coupling strength and conduction delay, suggesting that calibration is not necessary when the brain operates with a sub-graph solely connected via short-range connections while operating at maximal metastable state. The two symbols, * and *ns* represent significant (p<0.05) and non-significant changes, respectively.

When short-range (SR) connections are present in the network, we observe a strong association between the metastability heat maps of OA and Y_{SR+MR}, as well as Y_{SR} (Correlation of OA and Y_{SR+MR}=0.80 for CamCAN, 0.93 for Berlin; Correlation of OA andY_{SR}=0.78 for CamCAN, 0.76 for Berlin). However, when SR connections are absent in the network, specifically for the sub-graphs Y_{MR+LR} and Y_{LR}, the correlation of metastability maps between OA and these sub-graphs decreases (correlation of OA and Y_{MR+LR}=0.36 for CamCAN, 0.70 for Berlin; correlation of OA andY_{LR}=0.46 for CamCAN, 0.56 for Berlin). This suggests that SR connections emphasize a consistent metastability pattern similar to the OA, indicating that SR connections might play a significant role in driving the overall metastability of the network for older individuals. Arvin et al. also suggest that short-range connections are more important than long-range connections for metastability [Arvin et al., 2022].

3.5 Model-based parameter modulation

To identify the subject-specific biophysical characteristics contributing to maintaining functional integrity, global coupling strength (Fig. 6(c,d)), and conduction delay (Fig. 6(e,f)), we select optimal parameters conditioned on maximizing metastability, as described in the Methods section. The mean (standard deviation) values of optimal coupling strength and conduction delay are listed in Table 5. Figures 6(c) and 6(d) for the CamCAN and Berlin cohorts show the boxplots for optimal coupling strength, respectively. We observe a significant increase in the optimal coupling strength (κ) for older adults compared to younger groups in both datasets ($F(77)$=2.34, p<0.05 for CamCAN; Z=2.44, p<0.01 for Berlin). Increasing the coupling strength may be an adaptive process associated with the functional compensation for age-related long-range white-matter fiber loss [Petkoski et al., 2023].

Further, to investigate which specific sub-graph increases coupling strength in elderly cohorts, we compare the optimal κ estimated from the OA group with that of other sub-graph types. The optimal κ for Y_{SR+MR}, Y_{MR+LR}, and Y_{LR} significantly decrease compared to older adults (CamCAN: $F(69)$=-2.65, p<0.05 for Y_{SR+MR}; $F(71)$=-14, p<0.05 for Y_{MR+LR}; $F(70)$=-2.26, p<0.05 for Y_{LR}; Berlin: Y_{LR} for Z=3.17, p=0.001 for Y_{SR+MR}; Z=3.55, p=0.003 for Y_{MR+LR}; Z=2.1, p=0.05 for Y_{LR}). However, we find no significant difference between the optimal κ of OA and Y_{SR} (for both datasets), indicating that the optimal κ of sub-graphs containing SR connections is similar to that of optimal coupling strength of older adults, see Figs. 6(c,d).

Figure 6(e) for the CamCAN and Fig. 6(f) for Berlin cohorts show the box plots for optimal conduction delay (τ). We observe that the optimal conduction delay for the entire network remains unchanged for both young adult (YA) and older adult (OA) groups in both cohorts. The mean values of delays are very low for both groups. We find no significant difference between OA and Y_{MR+SR} for Cam-CAN and a significant difference for Berlin, indicating that the effects of sub-graphs containing short-range (SR) and mid-range (MR) connections on conduction delay are not evident. The optimal conduction delay significantly increases compared to OA when SR connections are removed from the anatomical network of young subjects (CamCAN: OA vs. Y_{MR+LR}, $F(71)$=12.63, p<0.05; Berlin: OA vs. Y_{MR+LR}, U=3.35, p<0.001). Additionally, there was a significant difference between OA and Y_{LR} for both cohorts (CamCAN: OA vs. Y_{LR}, $F(72)$=5.94, p<0.05; Berlin: OA vs. Y_{LR}, $F(72)$=5. However, there is no significant difference between OA and Y_{SR} for

both datasets, indicating that when the system has only SR connections, the conduction delay value is similar to that of the older cohorts. We find a consistent observation when comparing the coupling strength (and conduction delay) of older cohorts and the sub-graph solely connected via short-range fibers in both datasets.

Table 5: **Mean and standard deviation of optimal coupling strength and conduction delay for different sub-graph types.** We perform independent t-tests (for CamCAN) and Mann-Whitney U tests (for Berlin) to compare the optimal parameters between young adults (YA) and older adults (OA), as well as between OA and other sub-graphs. Significant differences are denoted by a star (*) in the superscript of the corresponding group, while non-significant changes are indicated by ns.

	YA mean(sd)	OA mean(sd)	Y_{SR+MR} mean(sd)	Y_{SR} mean(sd)	Y_{MR+LR} mean(sd)	Y_{LR} mean(sd)
CamCAN dataset						
optimal κ	26.59 (10.1)*	32.11 (9.6)	26.33 (8.5)*	30.10 (11.4)^{ns}	8.50 (2.6)*	27.34 (13.4)*
optimal τ	3.46 (2.0)^{ns}	3.53 (2.8)	2.69 (1.6) ^{ns}	2.72 (6.4)^{ns}	30.0 (12.1)*	18.84 (15.6)*
Berlin dataset						
optimal κ	20.25 (12.1)*	36.26 (10.1)	17.80 (12.3)*	37.71 (13.3)^{ns}	12.77 (12.4)*	30.01 (11.4)*
optimal τ	4.24 (3.1)^{ns}	4.76 (11.1)	23.08 (18.0)*	6.23 (14.1)^{ns}	22.81 (13.2)*	12.02 (16.0)*

4 Discussion

The study highlights the neurocompensatory mechanisms underlying the preservation of functional integrity in an aging brain governed by two sub-communities comprising short, long-range connections. Our study investigated sub-community inter-dependency in maintaining maximum metastability in young and elderly individuals. Particularly, we emphasized the important role of the SR community in maintaining desired brain dynamics to its target set point in the face of declined long-range fibers with age.

We observed overall white matter tract loss prominently in the long-range fibers, besides reorganization in functional connectivity in elderly cohorts. However, despite structural decline, the brain's dynamical complexity captured by metastability remains unaltered, indicating an age-related adaptive mechanism of neurocompensation. Our results suggested that both SR and LR communities contribute to preserving functional integrity but in different ways. In particular, SR connections readjust their coupling strength to compensate for the loss of long-range connections, whereas the LR community mainly contributes to the system's conduction delay. We provided a parsimonious explanation for the systematic enhancement of coupling strength with age by demonstrating a systematic reduction in long-range connectivity and the creation of new clusters with increased local short-range connectivity, which supports partial synchronization in the complex network. One possible reason for the indifference in brain dynamics compared to young adults could be the accelerated degeneration of long-range neural fibers resulting in over-activation at the whole brain level.

4.1 Anatomical alterations and functional reorganization with age

We categorized three sub-community networks based on the white matter tract lengths, which include short-range (SR), mid-range (MR), and long-range (LR) connections. SR connections are the most common type of connection, accounting for approximately 80% of the total connection strength in the structural topology. MR and LR strengths accounted for

14% and 6% of the total fiber strength, respectively. White matter tract loss is estimated to be approximately 35% for the CamCAN dataset and 11% for the Berlin dataset in elderly individuals. On average, the total counts of SR tracts are reduced by approximately 31% in elderly subjects, while the total strength of MR and LR connections is reduced by 64% and 78%, respectively. Furthermore, we observe that the total tract length is reduced by 13% in the CamCAN dataset (2% in the Berlin dataset) in the elder group. Interestingly, it is seen that the total SR tract length (6%) is reduced more than MR and LR length (2% and 3%, respectively). Our results indicate that aging is associated with a significant loss of white matter connections, particularly in MR and LR connections, with a more noticeable decline in long-range connections. LR loss may be higher since they are highly metabolically demanding [Bullmore and Sporns, 2012] and require more energy to maintain, making them more vulnerable to age-related atrophy [Meijer et al., 2020].

One of the fundamental constraints of coordinated dynamics and brain function is the anatomical topology [Pang et al., 2023]. Long-distance connections contribute to the brain's functional diversity and complexity, as highlighted by Betzel et al. ([Betzel and Bassett, 2018]. In that case, deterioration of the long-range white matter tracts may impair healthy brain dynamical repertoire. On the other hand, functional reorganization is a crucial aspect of the aging brain [Aron et al., 2022]. The process of preserving or altering the segregation, integration, and resilience of brain functions, allowing the brain to reorganize and maintain its overall effectiveness and functionality despite changes in structural topology, is called the functional integrity of the brain [Aron et al., 2022]. Significant alterations in connectivity weights, variability, segregation, and integration collectively demonstrate functional reorganization in aging. Reduced modularity, increased clustering, and increased path length with aging reflect the brain's reorganization in response to the challenges posed by aging, such as cognitive decline or sensor changes [Sala-Llonch et al., 2014, Song et al., 2014].

4.2 Preserved dynamical complexity in the aging brain

The term 'metastability' was popularized by Scott Kelso, who drew inspiration from the works of Rodalfo Linas and Fransisco Varela and his own brain-behavior experiments [Llinás, 1988, Kelso, 2012]. He expressed the metastability in the brain as a transient state where the whole-brain neural circuit has more opportunities to choose any attractor in response to external stimulus [Kelso, 2012]. Deco et al. demonstrated that the resting brain operates at maximum metastability [Deco et al., 2017]. This state can be interpreted as a state in which the brain's information processing capabilities are optimized, resulting in increased flexibility [Naik et al., 2017]. The dynamical working point of healthy aging has been suggested to lie within the regime of maximum metastability [Naik et al., 2017, Naskar et al., 2021]. Alterations in metastability have been observed in neuronal disorder, which is related to changes in dynamic repertories [Hellyer et al., 2015, Váša et al., 2015, Córdova-Palomera et al., 2017, Lee et al., 2018, Hancock et al., 2023], e.g., reduction in neural metastability linked to damage in the connectome and had behavioral implications [Hellyer et al., 2015], focal lesion could disrupt its anatomical architecture leading to alterations in metastability [Váša et al., 2015], decreased metastability in Alzheimer's [Córdova-Palomera et al., 2017] and increased salience network metastability in schizophrenia [Lee et al., 2018, Hancock et al., 2023]. The dynamical measure metastability can better indicate overall dynamical complexity while capturing functional integrity of the healthy aging brain. Our results show that metastability remains unchanged between the young and

old groups, obtained from individuals' resting state fMRI BOLD signals of CamCAN and Berlin datasets. Unaltered metastability indicates preserving information-processing abilities across the whole brain in the age cohorts. It allows switching and promptly reacting to internal or external stimuli.

4.3 Age-related neurocompensatory mechanism

One crucial facet of brain plasticity lies in its ability to establish new connections [Murphy and Corbett, 2009] and adjust underlying biophysical parameters, such as neurotransmitter modulation [Saha et al., 2023], in response to damage in brain topology. This process is often referred to as the brain's neurocompensatory mechanism [Lövdén et al., 2010, Pathak et al., 2022, Petkoski et al., 2023, Saha et al., 2023].

Our observations, based on personalized large-scale generative models in two independent datasets, point towards a neurocompensatory mechanism associated with aging, consistent with earlier reports by [Park and Reuter-Lorenz, 2009]. This mechanism is characterized by the reorganization of global functional organization and the preservation of dynamic complexity, as indicated by the unaltered metastability despite significant structural loss. Results revealed that the aging brain calibrates parameters to maintain dynamical complexity that sustains functional integrity despite long-range fiber deterioration. In particular, global coupling strength, which scales the local interaction strength among brain regions, is significantly modulated and primarily contributes to the neurocompensation, in line with prior observations in aging [Petkoski et al., 2023, Pathak et al., 2022]. Another recent study on epilepsy also found that biophysical parameters are crucial for optimizing desired working points [Courtiol et al., 2020]. Contrary to interaction strength, long-range connection-related conduction delay contributes less to the neurocompensatory process, which may be caused by long-range fiber loss.

4.4 Role of SR and LR sub-communities on neurocompensation

Further, we have highlighted the specific roles of the two sub-communities connected via short- and long-range tracts in modifying global interaction strength and conduction delay. In addition, the neurocompensation phenomena seen in healthy aging are explained mechanistically from the observations based on the subgraph analysis. Our results showed no significant shift at the optimal coupling strength when comparing the subgraph comprising solely short-range (SR) fibers with older adults (OA) but significant alterations with young adults (YA). We also noticed an important relationship between the metastability of OA and SR subgraph. These findings suggest that short-range connections modulate coupling strength in the aging brain to sustain the desired set point, keeping functional integrity intact.

We observed substantial shifts in the optimal delay in the sub-graph comprising long-range links. In contrast to the findings for coupling strength and short-range connections, the propagation delay seemed to have little influence on the neurocompensation in aging. This disparity could be explained by decreased long-range tract in older adults, resulting in a smaller effect on delay modulation. However, this effect is more pronounced in younger subjects and is a complex process controlled by a variety of variables, including brain activity, electrical and biochemical properties, as well as the

physical length, thickness, and myelination of the fibers, which is beyond the scope of our current investigation.

Short-range tracts (low-cost connections) can remarkably reduce energy and resource consumption when forming, utilizing, and maintaining brain connections [Raichle and Mintun, 2006]. Moreover, they play a pivotal role in developmental disorders [Ouyang et al., 2017], and act as the most efficient communication pathways across the whole brain [Mišić et al., 2015]. The presence of both hypo- and hyper-connectivity in short-range fibers has been identified during early childhood in individuals with Autism Spectrum Disorder (ASD) [Rudie and Dapretto, 2013] and schizophrenia [McGlashan and Hoffman, 2000]. The impairment of local connectivity in older adults and Alzheimer's Disease (AD) contributes to lower cognitive efficiency and consequently results in higher compensatory neuronal activity [Gao et al., 2014]. On the other hand, long-range white matter tracts, characterized by their myelinated fibers, play a crucial role in carrying long distant synapses across the brain that facilitate efficient and effective communication supporting various cognitive functions [Sporns and Zwi, 2004]. The scientific literature extensively investigates age-related loss of long-range white matter tracts and its subsequent impact on conduction velocity [Sullivan and Pfefferbaum, 2006, Bennett et al., 2010]. Thus, our observations on neurocompensatory mechanisms, separately driven by the short-range and long-range networks, could pave a new avenue toward developing interventions to maintain brain function in neurodevelopmental and neurodegenerative disorders.

4.5 Limitations

Several limitations in our study need to be addressed in future research. To begin with, the Kumamoto model captures the emerged phase dynamics of the neural signals in the whole brain. Instead, more realistic models could be utilized to gain further detailed insights into the underlying alterations in excitation-inhibition balance and neurotransmitter levels [Vattikonda et al., 2016, Naskar et al., 2021].

Furthermore, the network investigation was based on a coarse parcellation scheme comprising only 68 brain regions. However, our results will likely be validated using other high-resolution parcellations. Moreover, there are inherent limitations in tractography measures using diffusion MRI techniques, such as the failure to identify existing tracts in cross-hemispheric connectivity. It could be challenging to resolve accurately as the uncertainty in a streamlined location increases with the length of the tract.

Additionally, there are systematic differences in brain size, grey matter atrophy, and white matter hyperintensities with aging. However, more systematic explorations are required to incorporate them as free parameters in the model for all the network simulations. Future studies can be performed in particular to address this issue. Finally, it should be noted that while we use the Kuramoto order parameter, quantifying metastability captures the whole brain's dynamical repertoire, which only measures in-phase cohesion and its deviations. Other cohesion patterns, such as anti-phase or anti-synchrony, and their fluctuations are partially captured.

4.6 Conclusion

In summary, this study highlights the importance of short-range connections in compensating for long-range fiber loss by modulating the global coupling strength, which is crucial to maintaining functional integrity with aging. Brain networks can achieve optimal metastability by calibrating the parameters supported by the short-range connections. The intact metastability could be speculated as a compensatory mechanism of functional network reorganization with age, separately driven by the two subgraphs. The methodology provides a novel approach to studying the complex interplay between structural and functional brain networks, which can be applied further in investigating mechanisms underlying brain function in neural disorders.

Acknowledgments

We acknowledge the generous support of NBRC Core funds and the Computing facility. For simulations, resources from Neuroscience Gateway [Sivagnanam et al., 2013] were used. SS is supported by NPDF, SERB-DST, India, Award ID:PDF/2021/000585. AB acknowledge NBRC Flagship program, DBT, India, Award ID: BT/MED-III/NBRC/Flagship/Flagship2019. AB is supported by the Ministry of Youth Affairs and Sports, India, Award ID: F.NO.K-15015/42/2018/SP-V. DR is supported by Ramalingaswami Fellowship, DBT, India, Award ID:BT/RLF/Re-entry/07/2014 and DST, India, Award ID:SR/CSRI/21/2016.

Author contribution

PC: Data accusation; Conceptualization; Investigation; Methodology; Visualization; Writing original draft, Editing. SS: Conceptualization; Investigation; Methodology; Visualization; Writing original draft, Editing. AB: Methodology; Visualization; Funding acquisition; Supervision; Project Administration; Resources; Editing. DR: Conceptualization; Methodology; Visualization; Funding acquisition; Supervision; Project Administration; Resources; Writing original draft and editing.

Disclosure

The authors report no conflict of interest.

Data and Code Availability

This paper's analysis code is available on GitHub (https://github.com/dynamicdip/). Any data used in this paper are available from the corresponding author on reasonable request.

References

[Andersson et al., 2003] Andersson, J. L., Skare, S., and Ashburner, J. (2003). How to correct susceptibility distortions in spin-echo echo-planar images: application to diffusion tensor imaging. *Neuroimage*, 20(2):870–888.

[Aron et al., 2022] Aron, L., Zullo, J., and Yankner, B. (2022). The adaptive aging brain. *Current Opinion in Neurobiology*, 72:91–100.

[Arvin et al., 2022] Arvin, S., Glud, A. N., and Yonehara, K. (2022). Short-and long-range connections differentially modulate the dynamics and state of small-world networks. *Frontiers in Computational Neuroscience*, 15:124.

[Avena-Koenigsberger et al., 2017] Avena-Koenigsberger, A., Mišić, B., Hawkins, R. X., Griffa, A., Hagmann, P., Goñi, J., and Sporns, O. (2017). Path ensembles and a tradeoff between communication efficiency and resilience in the human connectome. *Brain Structure and Function*, 222(1):603–618.

[Bassett and Bullmore, 2006] Bassett, D. S. and Bullmore, E. (2006). Small-world brain networks. *The neuroscientist*, 12(6):512–523.

[Bassett and Bullmore, 2017] Bassett, D. S. and Bullmore, E. T. (2017). Small-world brain networks revisited. *The Neuroscientist*, 23(5):499–516.

[Bennett et al., 2010] Bennett, I. J., Madden, D. J., Vaidya, C. J., Howard, D. V., and Howard Jr, J. H. (2010). Age-related differences in multiple measures of white matter integrity: A diffusion tensor imaging study of healthy aging. *Human brain mapping*, 31(3):378–390.

[Betzel and Bassett, 2018] Betzel, R. F. and Bassett, D. S. (2018). Specificity and robustness of long-distance connections in weighted, interareal connectomes. *Proceedings of the National Academy of Sciences*, 115(21):E4880–E4889.

[Betzel et al., 2014] Betzel, R. F., Byrge, L., He, Y., Goñi, J., Zuo, X.-N., and Sporns, O. (2014). Changes in structural and functional connectivity among resting-state networks across the human lifespan. *Neuroimage*, 102:345–357.

[Breakspear et al., 2010] Breakspear, M., Heitmann, S., and Daffertshofer, A. (2010). Generative models of cortical oscillations: neurobiological implications of the kuramoto model. *Frontiers in human neuroscience*, 4:190.

[Bullmore and Sporns, 2009] Bullmore, E. and Sporns, O. (2009). Complex brain networks: graph theoretical analysis of structural and functional systems. *Nature reviews neuroscience*, 10(3):186–198.

[Bullmore and Sporns, 2012] Bullmore, E. and Sporns, O. (2012). The economy of brain network organization. *Nature reviews neuroscience*, 13(5):336–349.

[Cabral et al., 2011] Cabral, J., Hugues, E., Sporns, O., and Deco, G. (2011). Role of local network oscillations in resting-state functional connectivity. *Neuroimage*, 57(1):130–139.

[Coelho et al., 2021] Coelho, A., Fernandes, H. M., Magalhães, R., Moreira, P. S., Marques, P., Soares, J. M., Amorim, L., Portugal-Nunes, C., Castanho, T., Santos, N. C., et al. (2021). Signatures of white-matter microstructure degradation during aging and its association with cognitive status. *Scientific Reports*, 11(1):1–12.

[Córdova-Palomera et al., 2017] Córdova-Palomera, A., Kaufmann, T., Persson, K., Alnæs, D., Doan, N. T., Moberget, T., Lund, M. J., Barca, M. L., Engvig, A., Brækhus, A., et al. (2017). Disrupted global metastability and static and dynamic brain connectivity across individuals in the alzheimer's disease continuum. *Scientific reports*, 7(1):1–14.

[Courtiol et al., 2020] Courtiol, J., Guye, M., Bartolomei, F., Petkoski, S., and Jirsa, V. K. (2020). Dynamical mechanisms of interictal resting-state functional connectivity in epilepsy. *Journal of Neuroscience*, 40(29):5572–5588.

[Daffertshofer and van Wijk, 2011] Daffertshofer, A. and van Wijk, B. (2011). On the influence of amplitude on the connectivity between phases. *Frontiers in neuroinformatics*, 5:6.

[Dajani and Uddin, 2016] Dajani, D. R. and Uddin, L. Q. (2016). Local brain connectivity across development in autism spectrum disorder: A cross-sectional investigation. *Autism Research*, 9(1):43–54.

[Dale et al., 1999] Dale, A. M., Fischl, B., and Sereno, M. I. (1999). Cortical surface-based analysis: I. segmentation and surface reconstruction. *Neuroimage*, 9(2):179–194.

[Deco et al., 2019] Deco, G., Cruzat, J., Cabral, J., Tagliazucchi, E., Laufs, H., Logothetis, N. K., and Kringelbach, M. L. (2019). Awakening: Predicting external stimulation to force transitions between different brain states. *Proceedings of the National Academy of Sciences*, 116(36):18088–18097.

[Deco and Kringelbach, 2016] Deco, G. and Kringelbach, M. L. (2016). Metastability and coherence: extending the communication through coherence hypothesis using a whole-brain computational perspective. *Trends in neurosciences*, 39(3):125–135.

[Deco et al., 2017] Deco, G., Kringelbach, M. L., Jirsa, V. K., and Ritter, P. (2017). The dynamics of resting fluctuations in the brain: metastability and its dynamical cortical core. *Scientific reports*, 7(1):3095.

[Desikan et al., 2006] Desikan, R. S., Ségonne, F., Fischl, B., Quinn, B. T., Dickerson, B. C., Blacker, D., Buckner, R. L., Dale, A. M., Maguire, R. P., Hyman, B. T., et al. (2006). An automated labeling system for subdividing the human cerebral cortex on mri scans into gyral based regions of interest. *Neuroimage*, 31(3):968–980.

[Dhollander et al., 2018] Dhollander, T., Raffelt, D., and Connelly, A. (2018). Accuracy of response function estimation algorithms for 3-tissue spherical deconvolution of diverse quality diffusion mri data. In *Proceedings of the Joint Meeting of the European Society for Magnetic Resonance in Medicine and Biology and the International Society of Magnetic Resonance in Medicine, Paris, France*, volume 1569.

[Ercsey-Ravasz et al., 2013] Ercsey-Ravasz, M., Markov, N. T., Lamy, C., Van Essen, D. C., Knoblauch, K., Toroczkai, Z., and Kennedy, H. (2013). A predictive network model of cerebral cortical connectivity based on a distance rule. *Neuron*, 80(1):184–197.

[Gao et al., 2014] Gao, J., Cheung, R. T., Chan, Y.-S., Chu, L.-W., Mak, H. K., and Lee, T. M. (2014). The relevance of short-range fibers to cognitive efficiency and brain activation in aging and dementia. *PloS one*, 9(4):e90307.

[Grady et al., 2010] Grady, C. L., Protzner, A. B., Kovacevic, N., Strother, S. C., Afshin-Pour, B., Wojtowicz, M., Anderson, J. A., Churchill, N., and McIntosh, A. R. (2010). A multivariate analysis of age-related differences in default mode and task-positive networks across multiple cognitive domains. *Cerebral cortex*, 20(6):1432–1447.

[Hancock et al., 2023] Hancock, F., Rosas, F. E., McCutcheon, R. A., Cabral, J., Dipasquale, O., and Turkheimer, F. E. (2023). Metastability as a candidate neuromechanistic biomarker of schizophrenia pathology. *Plos one*, 18(3):e0282707.

[Hellyer et al., 2015] Hellyer, P. J., Scott, G., Shanahan, M., Sharp, D. J., and Leech, R. (2015). Cognitive flexibility through metastable neural dynamics is disrupted by damage to the structural connectome. *Journal of Neuroscience*, 35(24):9050–9063.

[Hellyer et al., 2014] Hellyer, P. J., Shanahan, M., Scott, G., Wise, R. J., Sharp, D. J., and Leech, R. (2014). The control of global brain dynamics: opposing actions of frontoparietal control and default mode networks on attention. *Journal of Neuroscience*, 34(2):451–461.

[Kana et al., 2011] Kana, R. K., Libero, L. E., and Moore, M. S. (2011). Disrupted cortical connectivity theory as an explanatory model for autism spectrum disorders. *Physics of life reviews*, 8(4):410–437.

[Kellner et al., 2016] Kellner, E., Dhital, B., Kiselev, V. G., and Reisert, M. (2016). Gibbs-ringing artifact removal based on local subvoxel-shifts. *Magnetic resonance in medicine*, 76(5):1574–1581.

[Kelso, 2012] Kelso, J. S. (2012). Multistability and metastability: understanding dynamic coordination in the brain. *Philosophical Transactions of the Royal Society B: Biological Sciences*, 367(1591):906–918.

[Kuramoto, 1984] Kuramoto, Y. (1984). *Chemical Oscillations, Waves, and Turbulence.*

[Latora and Marchiori, 2001] Latora, V. and Marchiori, M. (2001). Efficient behavior of small-world networks. *Phys. Rev. Lett.*, 87(19):198701.

[Lee et al., 2018] Lee, W. H., Doucet, G. E., Leibu, E., and Frangou, S. (2018). Resting-state network connectivity and metastability predict clinical symptoms in schizophrenia. *Schizophrenia research*, 201:208–216.

[Li et al., 2020] Li, X., Wang, Y., Wang, W., Huang, W., Chen, K., Xu, K., Zhang, J., Chen, Y., Li, H., Wei, D., et al. (2020). Age-related decline in the topological efficiency of the brain structural connectome and cognitive aging. *Cerebral cortex*, 30(8):4651–4661.

[Lim et al., 2015] Lim, S., Han, C. E., Uhlhaas, P. J., and Kaiser, M. (2015). Preferential detachment during human brain development: age-and sex-specific structural connectivity in diffusion tensor imaging (dti) data. *Cerebral Cortex*, 25(6):1477–1489.

[Llinás, 1988] Llinás, R. R. (1988). The intrinsic electrophysiological properties of mammalian neurons: insights into central nervous system function. *Science*, 242(4886):1654–1664.

[Lövdén et al., 2010] Lövdén, M., Bäckman, L., Lindenberger, U., Schaefer, S., and Schmiedek, F. (2010). A theoretical framework for the study of adult cognitive plasticity. *Psychological bulletin*, 136(4):659.

[Marder and Goaillard, 2006] Marder, E. and Goaillard, J.-M. (2006). Variability, compensation and homeostasis in neuron and network function. *Nature Reviews Neuroscience*, 7(7):563–574.

[McGlashan and Hoffman, 2000] McGlashan, T. H. and Hoffman, R. E. (2000). Schizophrenia as a disorder of developmentally reduced synaptic connectivity. *Archives of general psychiatry*, 57(7):637–648.

[Meijer et al., 2020] Meijer, K. A., Steenwijk, M. D., Douw, L., Schoonheim, M. M., and Geurts, J. J. (2020). Long-range connections are more severely damaged and relevant for cognition in multiple sclerosis. *Brain*, 143(1):150–160.

[Messé et al., 2014] Messé, A., Rudrauf, D., Benali, H., and Marrelec, G. (2014). Relating structure and function in the human brain: relative contributions of anatomy, stationary dynamics, and non-stationarities. *PLoS Comput Biol*, 10(3):e1003530.

[Mišić et al., 2015] Mišić, B., Betzel, R. F., Nematzadeh, A., Goni, J., Griffa, A., Hagmann, P., Flammini, A., Ahn, Y.-Y., and Sporns, O. (2015). Cooperative and competitive spreading dynamics on the human connectome. *Neuron*, 86(6):1518–1529.

[Murphy and Corbett, 2009] Murphy, T. and Corbett, D. (2009). Plasticity during stroke recovery: from synapse to behaviour. *Nature Reviews Neuroscience*, 10(12):861–872.

[Naik et al., 2017] Naik, S., Banerjee, A., Bapi, R. S., Deco, G., and Roy, D. (2017). Metastability in senescence. *Trends in cognitive sciences*, 21(7):509–521.

[Naskar et al., 2021] Naskar, A., Vattikonda, A., Deco, G., Roy, D., and Banerjee, A. (2021). Multi-scale dynamic mean field model (mdmf) relates resting-state brain dynamics with local cortical excitatory–inhibitory neurotransmitter homeostasis. *Network Neuroscience*, pages 1–55.

[Newman, 2002] Newman, M. E. (2002). Assortative mixing in networks. *Physical review letters*, 89(20):208701.

[Newman, 2003] Newman, M. E. (2003). Mixing patterns in networks. *Physical review E*, 67(2):026126.

[Newman, 2006] Newman, M. E. (2006). Modularity and community structure in networks. *Proc. of the Nat. Acad. of Sci.*, 103(23):8577–8582.

[Newman et al., 2006] Newman, M. E., Barabási, A.-L. E., and Watts, D. J. (2006). *The structure and dynamics of networks.* Princeton university press.

[Ouyang et al., 2017] Ouyang, M., Kang, H., Detre, J. A., Roberts, T. P., and Huang, H. (2017). Short-range connections in the developmental connectome during typical and atypical brain maturation. *Neuroscience & Biobehavioral Reviews*, 83:109–122.

[Oyefiade et al., 2018] Oyefiade, A. A., Ameis, S., Lerch, J. P., Rockel, C., Szulc, K. U., Scantlebury, N., Decker, A., Jefferson, J., Spichak, S., and Mabbott, D. J. (2018). Development of short-range white matter in healthy children and adolescents. *Human brain mapping*, 39(1):204–217.

[Pang et al., 2023] Pang, J. C., Aquino, K. M., Oldehinkel, M., Robinson, P. A., Fulcher, B. D., Breakspear, M., and Fornito, A. (2023). Geometric constraints on human brain function. *Nature*, pages 1–9.

[Pannese, 2011] Pannese, E. (2011). Morphological changes in nerve cells during normal aging. *Brain Structure and Function*, 216(2):85–89.

[Park and Reuter-Lorenz, 2009] Park, D. C. and Reuter-Lorenz, P. (2009). The adaptive brain: aging and neurocognitive scaffolding. *Annual review of psychology*, 60:173–196.

[Pathak et al., 2022] Pathak, A., Sharma, V., Roy, D., and Banerjee, A. (2022). Biophysical mechanism underlying compensatory preservation of neural synchrony over the adult lifespan. *Communications Biology*, 5(1):567.

[Peters, 2006] Peters, R. (2006). Ageing and the brain. *Postgraduate medical journal*, 82(964):84–88.

[Petkoski et al., 2023] Petkoski, S., Ritter, P., and Jirsa, V. K. (2023). White-matter degradation and dynamical compensation support age-related functional alterations in human brain. *Cerebral Cortex*. bhac500.

[Raichle and Mintun, 2006] Raichle, M. E. and Mintun, M. A. (2006). Brain work and brain imaging. *Annu. Rev. Neurosci.*, 29:449–476.

[Roalf et al., 2020] Roalf, D. R., Sydnor, V. J., Woods, M., Wolk, D. A., Scott, J. C., Reddy, R., and Moberg, P. J. (2020). A quantitative meta-analysis of brain glutamate metabolites in aging. *Neurobiology of aging*, 95:240–249.

[Rubinov and Sporns, 2010] Rubinov, M. and Sporns, O. (2010). Complex network measures of brain connectivity: uses and interpretations. *Neuroimage*, 52(3):1059–1069.

[Rudie and Dapretto, 2013] Rudie, J. D. and Dapretto, M. (2013). Convergent evidence of brain overconnectivity in children with autism? *Cell reports*, 5(3):565–566.

[Saha et al., 2023] Saha, S., Chakraborty, P., Naskar, A., Roy, D., and Banerjee, A. (2023). Neuromolecular interactions guiding homeostatic mechanisms underlying healthy ageing: A view from computational microscope. *bioRxiv*, pages 2023–03.

[Sala-Llonch et al., 2014] Sala-Llonch, R., Junqué, C., Arenaza-Urquijo, E. M., Vidal-Piñeiro, D., Valls-Pedret, C., Palacios, E. M., Domènech, S., Salvà, A., Bargalló, N., and Bartrés-Faz, D. (2014). Changes in whole-brain functional networks and memory performance in aging. *Neurobiology of aging*, 35(10):2193–2202.

[Salthouse, 2012] Salthouse, T. (2012). Consequences of age-related cognitive declines. *Annual review of psychology*, 63:201–226.

[Schirner et al., 2015] Schirner, M., Rothmeier, S., Jirsa, V. K., McIntosh, A. R., and Ritter, P. (2015). An automated pipeline for constructing personalized virtual brains from multimodal neuroimaging data. *NeuroImage*, 117:343–357.

[Shafto et al., 2014] Shafto, M. A., Tyler, L. K., Dixon, M., Taylor, J. R., Rowe, J. B., Cusack, R., Calder, A. J., Marslen-Wilson, W. D., Duncan, J., Dalgleish, T., et al. (2014). The cambridge centre for ageing and neuroscience (cam-can)

study protocol: a cross-sectional, lifespan, multidisciplinary examination of healthy cognitive ageing. *BMC neurology*, 14(1):1–25.

[Shanahan, 2010] Shanahan, M. (2010). Metastable chimera states in community-structured oscillator networks. *Chaos: An Interdisciplinary Journal of Nonlinear Science*, 20(1):013108.

[Shinn et al., 2023] Shinn, M., Hu, A., Turner, L., Noble, S., Preller, K. H., Ji, J. L., Moujaes, F., Achard, S., Scheinost, D., Constable, R. T., et al. (2023). Functional brain networks reflect spatial and temporal autocorrelation. *Nature Neuroscience*, pages 1–12.

[Sivagnanam et al., 2013] Sivagnanam, S., Majumdar, A., Yoshimoto, K., Astakhov, V., Bandrowski, A. E., Martone, M. E., Carnevale, N. T., et al. (2013). Introducing the neuroscience gateway. *IWSG*, 993:0.

[Smith et al., 2012] Smith, R. E., Tournier, J.-D., Calamante, F., and Connelly, A. (2012). Anatomically-constrained tractography: improved diffusion mri streamlines tractography through effective use of anatomical information. *Neuroimage*, 62(3):1924–1938.

[Smith et al., 2015] Smith, R. E., Tournier, J.-D., Calamante, F., and Connelly, A. (2015). Sift2: Enabling dense quantitative assessment of brain white matter connectivity using streamlines tractography. *Neuroimage*, 119:338–351.

[Song et al., 2014] Song, J., Birn, R. M., Boly, M., Meier, T. B., Nair, V. A., Meyerand, M. E., and Prabhakaran, V. (2014). Age-related reorganizational changes in modularity and functional connectivity of human brain networks. *Brain Connectivity*, 4(9):662–676.

[Sporns and Zwi, 2004] Sporns, O. and Zwi, J. D. (2004). The small world of the cerebral cortex. *Neuroinformatics*, 2:145–162.

[Sullivan and Pfefferbaum, 2006] Sullivan, E. V. and Pfefferbaum, A. (2006). Diffusion tensor imaging and aging. *Neuroscience & Biobehavioral Reviews*, 30(6):749–761.

[Sullivan et al., 2010] Sullivan, E. V., Rohlfing, T., and Pfefferbaum, A. (2010). Quantitative fiber tracking of lateral and interhemispheric white matter systems in normal aging: relations to timed performance. *Neurobiology of aging*, 31(3):464–481.

[Surampudi et al., 2019] Surampudi, S. G., Misra, J., Deco, G., Bapi, R. S., Sharma, A., and Roy, D. (2019). Resting state dynamics meets anatomical structure: Temporal multiple kernel learning (tmkl) model. *NeuroImage*, 184:609–620.

[Taylor et al., 2017] Taylor, J. R., Williams, N., Cusack, R., Auer, T., Shafto, M. A., Dixon, M., Tyler, L. K., Henson, R. N., et al. (2017). The cambridge centre for ageing and neuroscience (cam-can) data repository: Structural and functional mri, meg, and cognitive data from a cross-sectional adult lifespan sample. *neuroimage*, 144:262–269.

[Tournier et al., 2019] Tournier, J.-D., Smith, R., Raffelt, D., Tabbara, R., Dhollander, T., Pietsch, M., Christiaens, D., Jeurissen, B., Yeh, C.-H., and Connelly, A. (2019). Mrtrix3: A fast, flexible and open software framework for medical image processing and visualisation. *Neuroimage*, 202:116137.

[Tustison et al., 2010] Tustison, N. J., Avants, B. B., Cook, P. A., Zheng, Y., Egan, A., Yushkevich, P. A., and Gee, J. C. (2010). N4itk: improved n3 bias correction. *IEEE transactions on medical imaging*, 29(6):1310–1320.

[Uddin, 2021] Uddin, L. Q. (2021). Cognitive and behavioural flexibility: neural mechanisms and clinical considerations. *Nature Reviews Neuroscience*, 22(3):167–179.

[Van Den Heuvel and Sporns, 2011] Van Den Heuvel, M. P. and Sporns, O. (2011). Rich-club organization of the human connectome. *Journal of Neuroscience*, 31(44):15775–15786.

[Váša et al., 2015] Váša, F., Shanahan, M., Hellyer, P. J., Scott, G., Cabral, J., and Leech, R. (2015). Effects of lesions on synchrony and metastability in cortical networks. *Neuroimage*, 118:456–467.

[Vattikonda et al., 2016] Vattikonda, A., Surampudi, B. R., Banerjee, A., Deco, G., and Roy, D. (2016). Does the regulation of local excitation–inhibition balance aid in recovery of functional connectivity? a computational account. *Neuroimage*, 136:57–67.

[Veraart et al., 2016] Veraart, J., Novikov, D. S., Christiaens, D., Ades-Aron, B., Sijbers, J., and Fieremans, E. (2016). Denoising of diffusion mri using random matrix theory. *Neuroimage*, 142:394–406.

[Veríssimo et al., 2022] Veríssimo, J., Verhaeghen, P., Goldman, N., Weinstein, M., and Ullman, M. T. (2022). Evidence that ageing yields improvements as well as declines across attention and executive functions. *Nature Human Behaviour*, 6(1):97–110.

[Watts and Strogatz, 1998] Watts, D. J. and Strogatz, S. H. (1998). Collective dynamics of 'small-world'networks. *nature*, 393(6684):440–442.

[Whitfield-Gabrieli and Nieto-Castanon, 2012] Whitfield-Gabrieli, S. and Nieto-Castanon, A. (2012). Conn: a functional connectivity toolbox for correlated and anticorrelated brain networks. *Brain connectivity*, 2(3):125–141.

[Wu et al., 2014] Wu, M., Lu, L. H., Lowes, A., Yang, S., Passarotti, A. M., Zhou, X. J., and Pavuluri, M. N. (2014). Development of superficial white matter and its structural interplay with cortical gray matter in children and adolescents. *Human brain mapping*, 35(6):2806–2816.